Robust Control Design for the Flying-V within the Signal-Based H-infinity Framework

Pedroso, Beatriz; Pollack, T.S.C.; Theodoulis, Spilios

DOI
10.2514/6.2026-1952

Publication date
2026

Document Version
Final published version

Published in
Proceedings of the AIAA SCITECH 2026 Forum

AIAA SciTech Forum
12-16 January 2026, Orlando, FL
AIAA SCITECH 2026 Forum

10.2514/6.2026-1952

Robust Control Design for the Flying V Aircraft within the Signal-Based $\mathcal{H}_\infty$ Framework

Beatriz Pedroso * Tijmen Pollack † and Spilios Theodoulis ‡
Delft University of Technology, Delft, 2629HS, Netherlands

The Flying V concept aircraft represents a notable candidate to reduce the carbon footprint of the aviation industry, with a potential 20% decrease in fuel use and a 17% higher lift-over-drag ratio. However, given the inherent design limitations concerning low control authority and pitch break-up tendencies, a well-designed control system is crucial for the aircraft's safe operation. Thus, this study proposes a systematic design and tuning of a digital longitudinal flight control system that explicitly addresses robustness specifications a-priori. The flight dynamics simulation modeling is first detailed, followed by the outline and discussion of the design specifications. A C* longitudinal control law is designed using a signal-based $\mathcal{H}_\infty$ framework. Results indicate effective disturbance and noise rejection, stability under parametric uncertainties, Level 1 handling qualities, and satisfactory performance in the nonlinear model. These results validate the control law's effectiveness, paving the way for future enhancements in gain-scheduled controllers for the Flying V.

I. Introduction

As the aviation industry faces growing environmental and societal pressures to decarbonize the sector and to be in line with the net-zero carbon emissions by 2050 target *, the need for innovative aircraft designs that prioritize energy efficiency and sustainability has become more paramount than ever. Consequently, novel concepts such as the FLYING V™†‡ (see Fig. 1§), currently researched by TU Delft, are critically important for a more sustainable future for aviation. An asymptote seems to have been reached in the conventional configurations in terms of aerodynamic efficiency gains [1]. Hence, the Flying V concept emerges as a promising alternative. The configuration was proposed in 2015 as a flying wing with a V-shaped passenger cabin [2]. Preliminary assessments by Benad and Vos [3] suggest that the Flying V could achieve a 20% lower fuel burn when compared to the state-of-the-art reference aircraft performing the same mission and with the same capacity and wingspan. Additionally, further analyses indicate that the Flying V achieves a 17% higher maximum trimmed lift-over-drag ratio when compared to the reference aircraft [4]. However, its unconventional shape and layout pose unique challenges in terms of stability and control, necessitating the development of advanced control systems.

Flight control system (FCS) design for the Flying V concept aircraft has been an active field in recent years. Some basic design methods were used to evaluate handling qualities (HQ), which include classical proportional-integral-derivative controllers (PIDs) and a direct law [5] as well as an adapted control allocation and a stability augmentation system (SAS) [6]. Furthermore, Völker et al. [7] developed a single-loop altitude controller using the reinforcement learning approach Twin-Delayed Deep Deterministic Policy Gradient. It allows offline learning which mitigates the danger of the system trying unsafe control signals during the learning phase. Lastly, several nonlinear approaches were also considered. van Overeem et al. [8] implemented a sensor-based Incremental Nonlinear Dynamic Inversion (INDI) FCS, followed by the research conducted by Stougie et al. [9], which also focused on an INDI implementation with flight envelope protections. Additionally, Traas [10] proposed an Hybrid INDI controller, which combines sensor-based and model-based information. Lastly, Atmaca and Kampen [11] proposed an adaptive strategy for INDI which employs an online two-step method that estimates changes in the aircraft's control effectiveness in order to minimize the mismatch between the actual and the onboard representation of the model.

*MSc Student, Control & Simulation department, Faculty of Aerospace Engineering, 2629HS Delft, Netherlands
†Postdoctoral Researcher, Aerospace Structures and Materials department, Faculty of Aerospace Engineering, 2629HS Delft, Netherlands
‡Associate Professor, Control & Simulation department, Faculty of Aerospace Engineering, 2629HS Delft, Netherlands. Associate Fellow AIAA
*https://www.iea.org/energy-system/transport/aviation. Accessed in November 2025
†Flying V is a trademark of Fortescue
‡The Flying V design is owned by Fortescue, UK & NL patents pending
§https://www.tudelft.nl/en/ae/Flying V. Accessed in November 2025

On the one hand, INDI and its variants have been a central focus in the Flying V FCS development with several advantages pointed out, namely the guarantee of closed-loop stability and the natural handling of nonlinear systems, which aims to alleviate the time-consuming process of gain scheduling. On the other hand, multivariable robust control is foundational to systematic tuning of control laws that are widely used in industry. However, despite its strengths, $\mathcal{H}_\infty$ control has not yet been applied to the Flying V.

Indeed, $\mathcal{H}_\infty$ control is a systematic framework that explicitly addresses robustness and performance specifications in the presence of plant model uncertainties and which does not necessarily require a predefined controller structure, contrarily to the INDI-based control laws. In fact, $\mathcal{H}_\infty$ control problem solutions obtained via Algebraic Ricatti Equations [12] and Linear Matrix Inequalities [13] result in full-order controllers. Nevertheless, as these might be impractical for implementation in industry due to hardware and software constraints and lack of transparency, tools for structured $\mathcal{H}_\infty$ synthesis were recently developed. These leverage the investigations conducted on non-smooth optimizers [14] to directly tune any single or multiple loop control architecture. The MATLAB® function `hinfstruct` became available to the general public in 2011 [15], allowing the structured controllers, such as PIDs, to be optimized instead of tuned [16]. Furthermore, multiple extensions were developed and incorporated into MATLAB® function `systune` [16]. Some include multi-objective $\mathcal{H}_2/\mathcal{H}_\infty$ synthesis [17], systematic tuning of gain scheduled control systems [18], and parametric robust $\mathcal{H}_\infty$ control [19]. Therefore, with the advent of these commercially available tools, robust control theory can be used to its full potential to tackle challenging control problems. In addition, by allowing structured controllers to be tuned directly against explicit performance and robustness requirements, these tools enable HQ criteria to be incorporated early in the design process. As a result, pilot-centric metrics, traditionally evaluated late in the development cycle can be embedded directly into the synthesis process, ensuring that both robustness objectives and HQ standards are simultaneously satisfied.

Additionally, in spite of their advantages, the INDI methods also have its drawbacks that can be addressed with a robust control design. To begin with, sensor-based INDI uses direct sensor measurements of the controlled variable derivatives and, thus, circumvents the need for accurate airframe models. Therefore, when compared to the classical model-based NDI, it is more robust against regular perturbations arising from aerodynamic variations [20]. However, in [20], the robustness properties are analysed via the open loop responses of sensor- and model-based linear dynamic inversion schemes with the same control law controller. It was demonstrated that the sensor-based inversion schemes result in higher open loop gain at low frequencies but unfortunately also in higher and often prohibitive crossover frequencies, which penalizes robustness at high frequencies due to insufficient roll-off [20]. Therefore, a known challenge for the sensor-based INDI control laws involves the high sensitivity to sensor measurement noise, time delays, and unmodeled HF dynamics [21]. Furthermore, contrarily to the $\mathcal{H}_\infty$ methods, there are little a-priori guarantees of robustness, only of nominal performance, in the design phase of dynamic inversion-based controllers [22] [23]. Additionally, while these inversion-based methods are the result of a time-domain design, robust control techniques allow to naturally and systematically treat plant model uncertainty in the frequency domain [23]. Ongoing efforts to combine the advantages of both the nonlinear and the robust approaches for the Flying V are observed with the work developed by Shahin [24]. It consists of a multi-loop μ-optimal approach to design a robust inversion-based control system, which was applied to the short period (SP) approximation of the longitudinal dynamics. Thus, robust control techniques are merged with previous design configurations, which shed light on the importance of $\mathcal{H}_\infty$ tools for robust stability and performance.

Therefore, the current research proposes a systematic design and tuning of a longitudinal flight control system tailored for the Flying V aircraft. It offers a scalable solution that explicitly addresses robustness specifications a-priori, contrarily to the structurally constrained methods that were previously applied to the concept aircraft. A C^* longitudinal control law is implemented and tuned within the signal-based $\mathcal{H}_\infty$ robust control framework. The suggested solution guarantees robustness against disturbances, measurement noise, sensor measurement time delays, and uncertainties in the model while ensuring performance and compliance with Level 1 HQ. Moreover, this paper is an extension to the work developed by Pedroso et al. [25] in terms of an improved FCS structure and of the development of a digital FCS and multi-model design.

This paper is structured as follows: Section II describes the Flying V concept, the mathematical nonlinear simulation model of the aircraft, and the process to obtain local linearized models, Section III details the design requirements, FCS structure, and optimization procedure for the control law tuning, and lastly, Section IV presents simulations results in the linear and nonlinear domains using nominal and uncertain models.

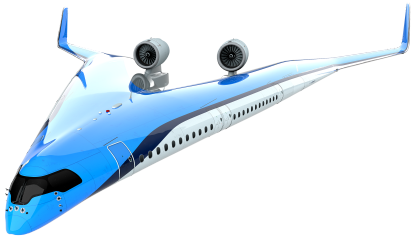

Fig. 1 Flying V concept aircraft.

II. Simulation Model

A. Flying V Aircraft Concept

The Flying V-1000 is the base model for this research and it is illustrated in Fig. 1. The relevant dimensions and parameters of this concept aircraft are summarized in Table 1, whose values are retrieved from the research developed by Cappuyns [26], Rubio Pascual [27], van der Pluijm [28], van Overeem et al. [29], and Oosterom and Vos [30].

Table 1 Flying V parameters.

Parameter	Value	Parameter	Value
Length	57 m	Forward center of gravity, CoG	29.372 m
Height	17 m	Motor displacement from CoG in x-axis, T_{d_x}	8.028 m
Wingspan, b	65 m	Motor displacement from CoG in y-axis, T_{d_y}	5.7 m
Chord, c	24 m	Motor displacement from CoG in z-axis, T_{d_z}	0.8 m
Wing area, S	898 m^2	Pilot station position in x-axis (PS) x_{PS}	6.7 m
Fuel capacity	140000 litres	Nose position in x-axis x_{nose}	1.5 m
Cargo capacity	160 m^3	Number of passengers	361

B. Nonlinear Model

The Flying V model is implemented in MATLAB® and Simulink®, with the main model workflow illustrated in Fig. 2. Each subsystem, namely the actuator dynamics, the aerodynamics, equations of motion (EoM), and the sensors, is further discussed in the current section.

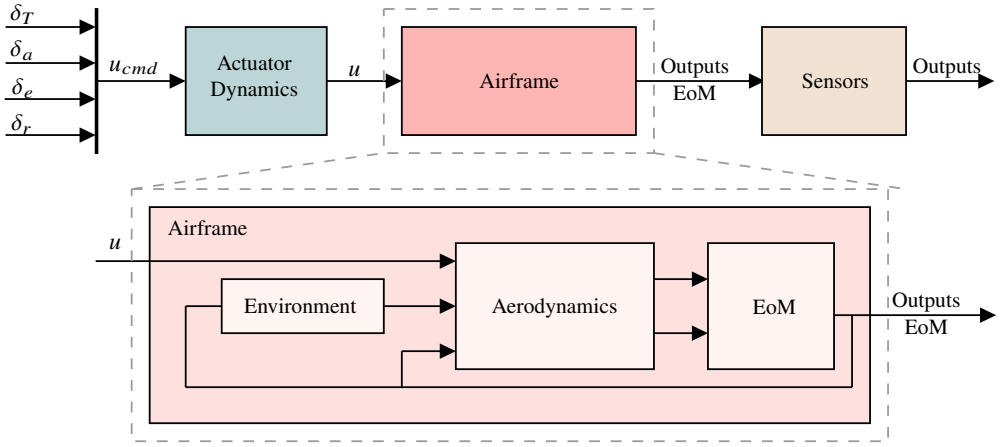

Fig. 2 Overview of *Simulink*'s Flying V model.

1. Aerodynamic Model

To compute the forces and moments acting on the aircraft, which are consequently used in the EoM, aerodynamic data is needed. This data was generated with Reynolds-Averaged Navier–Stokes (RANS) based computational fluid dynamics (CFD) simulations. The global values for the coefficients are given as a function of other variables, which include the angle of attack, α, the angle of sideslip, β, the dimensionless angular rates, $\hat{p}, \hat{q}, \hat{r}$, the control surface deflections, $\delta_a, \delta_e, \delta_r$, and the CoG location. These coefficients were provided for a total of sixteen flight conditions, which are dependent on the Mach number, M_a, and altitude. Therefore, the aerodynamic forces and moments coefficients are obtained by interpolating the global coefficients and by using the expressions represented in Eq. 1.

$$
\begin{aligned}
C_x =& C_{x_\alpha}(M_a, h, \alpha) + C_{x_{\delta_e}}(M_a, h, \delta_e) \\
C_y =& C_{y_\beta}(M_a, h, \beta) + C_{y_r}(M_a, h, r, CoG) + C_{y_{\delta_a}}(M_a, h, \delta_a) + C_{y_{\delta_r}}(M_a, h, \delta_r) \\
C_z =& C_{z_\alpha}(M_a, h, \alpha) + C_{z_q}(M_a, h, q) + C_{z_{\delta_e}}(M_a, h, \delta_e) \\
C_l =& C_{l_\beta}(M_a, h, \beta) + C_{l_p}(M_a, h, p) + C_{l_r}(M_a, h, r, CoG) + C_{l_{\delta_a}} + C_{l_{\delta_r}}(M_a, h, \delta_r) \\
C_m =& C_{m_\alpha}(M_a, h, \alpha, CoG) + C_{m_q}(M_a, h, q, CoG) + C_{m_{\delta_e}}(M_a, h, \delta_e, CoG) \\
C_n =& C_{n_\beta}(M_a, h, \beta, CoG) + C_{n_p}(M_a, h, p, CoG) + C_{n_r}(M_a, h, r, CoG) + \\
&+ C_{n_{\delta_a}}(M_a, h, \delta_a, CoG) + C_{n_{\delta_r}}(M_a, h, \delta_r, CoG)
\end{aligned} \tag{1}
$$

The total aerodynamic forces and moments are calculated as:

$$
\begin{bmatrix} F_{x_a} \\ F_{y_a} \\ F_{z_a} \end{bmatrix} = \bar{q}S \begin{bmatrix} C_x \\ C_y \\ C_z \end{bmatrix} \qquad \begin{bmatrix} M_{x_a} \\ M_{y_a} \\ M_{z_a} \end{bmatrix} = \bar{q}S \begin{bmatrix} bC_l \\ cC_m \\ bC_n \end{bmatrix} \tag{2}
$$

where $\bar{q} = 1/2\rho V^2$ is the dynamic pressure. Moreover, the propulsion and gravity forces are added to get the overall force acting on the aircraft. Additionally, the thrust contribution to the moments is also considered, since the engines are displaced from the CoG, as mentioned in section II.A.

2. Equations of Motion

The EoM are derived in a tensor-based formulation, which is highly advantageous to generalize the equations and to project these into the desired coordinate system. This is possible because tensors hold the physical characteristics and remain unaffected by the choice of a coordinate system. The derivation of the EoM are based on [31]. In terms of notation, scalars (zeroth-order tensors) are represented by lower-case characters, vectors (first-order tensors) are represented by bold lower-case characters, and tensors (second-order tensors) by bold upper-case characters.

The 6 degree of freedom simulation is implemented assuming a flat Earth model and allows to fully model the three translational and angular accelerations, velocities, and positions from the forces and moments acting on the system. The simulation supposes in-atmosphere and near-Earth flight, the North-East-Down (NED) reference frame is used, and both the mass and CoG location are assumed constant. The EoM are implemented and can be sub-categorized into four main parts, namely attitude and translational dynamics and attitude and translational kinematics. These are briefly explained in the current subsection.

Attitude Dynamics

Attitude dynamics formulate the attitude equations, which are governed by Euler's law. It states that the time rate of change of angular momentum is equal to the moments applied externally, $\boldsymbol{m}_B$. By expressing D^E, the rotational derivative in the Earth frame E, in the body frame B with Euler's transformation and applying the chain rule, the following expression is obtained:

$$
D^E\left(\boldsymbol{I}_B^B \boldsymbol{\omega}^{BE}\right) = \boldsymbol{m}_B \;\Leftrightarrow\; \underbrace{D^B \boldsymbol{I}_B^B}_{=0 \text{ for a rigid body}} \boldsymbol{\omega}^{BE} + \boldsymbol{I}_B^B D^B \boldsymbol{\omega}^{BE} + \boldsymbol{\Omega}^{BE} \boldsymbol{I}_B^B \boldsymbol{\omega}^{BE} = \boldsymbol{m}_B, \tag{3}
$$

where $\boldsymbol{I}_B^B$ is the moment of inertia of the aircraft body frame B referred to the center of mass (CoM) B and D^B is the rotational derivative in frame B. Additionally, $\boldsymbol{\omega}^{BE}$ and $\boldsymbol{\Omega}^{BE}$ are represented in Eq. (4).

$$
\left[\omega^{BE}\right]^B = \begin{bmatrix} p \\ q \\ r \end{bmatrix} \quad \text{and} \quad \left[\Omega^{BE}\right]^B = \begin{bmatrix} 0 & -r & q \\ r & 0 & -p \\ -q & p & 0 \end{bmatrix}. \tag{4}
$$

Lastly, Eq. (3) is projected into the body coordinate system, resulting in Eq. (5).

$$
\left[\frac{\mathrm{d}\omega^{BE}}{dt}\right]^B = \left(\left[I_B^B\right]^B\right)^{-1}\left(-\left[\Omega^{BE}\right]^B\left[I_B^B\right]^B\left[\omega^{BE}\right]^B + \left[m_B\right]^B\right), \tag{5}
$$

Translational Dynamics

Moreover, the translational dynamics are derived from Newton's second law with respect to the inertial frame which, for the flat-Earth assumption, leads to:

$$mD^I \boldsymbol{v}_B^I = \boldsymbol{f}_{a,p} + m\boldsymbol{g} \iff mD^E \boldsymbol{v}_B^E = \boldsymbol{f}_{a,p} + m\boldsymbol{g}, \tag{6}$$

where m is the aircraft mass, $\boldsymbol{v}_B^I$ ($= \boldsymbol{v}_B^E$) is the velocity of the vehicle CoM in frame B wrt the inertial frame I (which is assumed to be earth frame E), $\boldsymbol{f}_{a,p}$ are the subjected aerodynamic and propulsion forces, and $\boldsymbol{g}$ is the gravity term. Although in [31] the body frame was the chosen coordinate system, the wind frame coordinate system is the most adequate since the relevant states (V and α) can be directly used in the linearization without recurring to any approximations. This derivation in the wind framework was conducted in [32]. The most important steps are described. To begin with, by employing the Euler transformation twice, Eq. (6) was transformed to the wind frame W:

$$m\left(D^W \boldsymbol{v}_B^E + \boldsymbol{\Omega}^{WB} \boldsymbol{v}_B^E\right) + m\boldsymbol{\Omega}^{BE} \boldsymbol{v}_B^E = \boldsymbol{f}_{a,p} + m\boldsymbol{g}, \tag{7}$$

All terms are transformed into the coordinate system $]^W$ and the unknown body rates and forces in the wind coordinate system are transformed into known representations, as detailed in the under-brace descriptions:

$$m\left[\frac{\mathrm{d}v_B^E}{dt}\right]^W + m\left[\Omega^{WB}\right]^W \left[v_B^E\right]^W + m \underbrace{\left[\Omega^{BE}\right]^W}_{[T]^{WB}\left[\Omega^{BE}\right]^B} \underbrace{\left[v_B^E\right]^W}_{[\bar{T}]^{WB}} = \underbrace{\left[f_{a,p}\right]^W}_{[T]^{WB}\left[f_{a,p}\right]^B} + m \underbrace{[g]^W}_{[T]^{BL}[g]^L}, \tag{8}$$

where $\left[\frac{\mathrm{d}v_B^E}{dt}\right]^W$ corresponds to the change in velocity of the aircraft body wrt Earth in the wind axis, $\left[\Omega^{WB}\right]^W$ represents the angular rates of the wind to the body frames in the wind coordinate system, and $[T]^{WB}$ is the transformation matrix from the body to the wind coordinate systems. The skew-symmetric tensor $\left[\Omega^{WB}\right]^W$ is dictated by the derivatives $\dot{\alpha}$ and $\dot{\beta}$. Thus, the expression was solved for $\dot{V}, \dot{\alpha}$, and $\dot{\beta}$, concluding the derivation of the most important steps of the translational dynamics. It should be noted that zero wind conditions are assumed.

Attitude Kinematics

Furthermore, the body attitudes are retrieved from the body rates using the transformation matrix between the Euler angles and the body frame, as derived in [31]:

$$\begin{bmatrix} \dot{\phi} \\ \dot{\theta} \\ \dot{\psi} \end{bmatrix} = \begin{bmatrix} 1 & \sin\phi\tan\theta & \cos\phi\tan\theta \\ 0 & \cos\phi & -\sin\phi \\ 0 & \sin\phi\cos\theta & \cos\phi/\cos\theta \end{bmatrix} \begin{bmatrix} p \\ q \\ r \end{bmatrix} \tag{9}$$

Translational Kinematics

The location of the aircraft's CoM in frame B wrt an Earth reference point E, s_{BE}, is obtained by integrating twice the differential equations of the velocity vector (Translational Dynamics subsystem output), which are described as:

$$\begin{aligned} \dot{u} &= \dot{V}\cos\alpha\cos\beta - V\dot{\alpha}\cos\beta\sin\alpha - V\dot{\beta}\cos\alpha\sin\beta \\ \dot{v} &= \dot{V}\sin\beta + V\dot{\beta}\cos\beta \\ \dot{w} &= \dot{V}\cos\beta\sin\alpha + V\dot{\alpha}\cos\alpha\cos\beta - V\dot{\beta}\sin\alpha\sin\beta \end{aligned} \tag{10}$$

Hence, $\left[D^E s_{BE}\right] = \left[v_B^E\right]$. Furthermore, the integration was carried out in the local-level coordinate system, $]^L$, as expressed in Eq. (11).

$$\left[\frac{\mathrm{d}s_{BE}}{dt}\right]^L = \left[\bar{T}\right]^{BL}\left[v_B^E\right]^B \tag{11}$$

The six first-order differential equations that are fundamental to the motion of the aircraft with the Earth as the inertial reference frame are, now, completely obtained.

3. Actuator Dynamics

The Flying V possesses several elevons on the trailing edges. As the control surface sizing is still under development, the aerodynamic data used in the simulation accounts for a single elevon on each side that functions both as an elevator and an aileron. Additionally, there is also a rudder located on each side of the wing's back. In terms of aerodynamic data, the contributions of both rudders are presented as a single one. These control surfaces are modeled by a first order linear system with a time constant of 0.07 seconds and complemented with position and rate saturations.

4. Sensors

For the normal acceleration measurement, an inertial measurement unit (IMU) is used. However, in case it is displaced from the CoM, additional corrections need to be taken into consideration. This transformation was addressed by Grubin and, thus, it carries his name [31] (see Eq. (12)). It describes the relation between the sensor acceleration, a_{B_s}, and the acceleration of the body in the CoM, a_B, wrt an inertial frame point I. Additionally, $\boldsymbol{s}_{BB_s}$ corresponds to the position vector from the sensor to the CoM.

$$\boldsymbol{a}^I_{B_s} = \boldsymbol{a}^I_B - \Big(\underbrace{D^I\boldsymbol{\Omega}^{BI}\boldsymbol{s}_{BB_s}}_{\text{angular acceleration}} + \underbrace{\boldsymbol{\Omega}^{BI}\boldsymbol{\Omega}^{BI}\boldsymbol{s}_{BB_s}}_{\text{centrifugal acceleration}} \Big) \tag{12}$$

Nonetheless, it is important to note that the accelerometer is a specific force measuring device [33]. Therefore, the magnitude of the true force acting on the accelerometer is equal to the accelerometer weight and has a negative direction to the gravity vector derived from the reaction of the surface where it is applied [33]. Moreover, conventionally, the load factor, n_z, should have the opposite sign of the normal acceleration and, in the steady wings-level condition, it should measure +1 g-unit. Thus, to compute n_z, the standard gravity compensation factor ($[T]^{BL}[g]^L$) is subtracted from the acceleration value and the expression is multiplied by $-1/g_0$. Additionally, since a C^* control law will be designed (please refer to section III), the value of n_z also needs to be captured in the PS. Hence, Grubin's transformation can be applied analogously, where B_r and B correspond to the accelerometer and the PS positions, respectively.

Furthermore, the choice of sensors location plays an integral role in the aircraft design since the IMU detects not only the rigid-body motion but also higher frequency signal content. These create unstable structural coupling characteristics if passed through the FCS [34]. Although no aero-elasticity effects are considered, the location of the sensor was defined to be slightly in front of the instantaneous centre of rotation (ICR). This location is assumed to have limited sensitivity to structural coupling and other high frequency (HF) sources and avoids non-minimum phase (NMP) behaviours. The ICR locations for several flight conditions were calculated, resulting in the placement of the sensor at a distance of 7.2 meters from the CoG, towards the nose. A more in-depth investigation should be conducted for the Flying V.

C. Trimming and Linearization

1. Trimming Methodology

The accuracy of the linearized model is highly dependent on the accuracy of the trimming, provided that the linear approximations describe small perturbations around a certain trim condition. The trimming procedure computed the equilibrium points around an imposed condition $\boldsymbol{\rho}(t) = \bar{\boldsymbol{\rho}} = [\bar{M}_a \ \bar{h}]^T$ to zero out the forces and moments contribution of the body and control surfaces. The EoM can be represented in a general parameter-dependent form as:

$$\begin{cases} \dot{\mathbf{x}}(t) = \mathbf{f}_x[\mathbf{x}(t), \mathbf{u}(t), \boldsymbol{\rho}(t)], \ \ t \in \Re_+ \\ \mathbf{y}(t) = \mathbf{f}_y[\mathbf{x}(t), \mathbf{u}(t), \boldsymbol{\rho}(t)] \end{cases} \tag{13}$$

where $\mathbf{x} = [p\ q\ r\ \phi\ \theta\ \psi\ V\ \alpha\ \beta\ x_L\ y_L\ z_L]^T$ represents the state vector, $\mathbf{u} = [T\ \delta_a\ \delta_e\ \delta_r]^T$ is the control input vector, and $\mathbf{y} = [n_x\ n_y\ n_z\ p\ q\ r]^T$ is the output vector. The aircraft is in equilibrium if $\dot{\mathbf{x}}(t) \triangleq 0$. Solving this condition assumes that there are as many algebraic equations as unknown variables, which is not the case.

Thus, it is fundamental to address which variables can be chosen independently and what constraints exist on the remaining state and control variables. Firstly, the control variables (thrust and control surface deflections) must be adjusted by the trimming algorithm. Secondly, the NED altitude can be predefined, since the trimming flight conditions depend on this state and the Mach number. The other two position states are not relevant. Additionally, for steady wings-level flight, we can consider that the roll angle, ϕ, and the angular rates, p, q, r, are null. The yaw angle, ψ, can be specified freely. Nonetheless, the sideslip angle, β, must be adjusted by the algorithm, in case a side force

has to be counteracted. Hence, only the states V, α, and θ remain to be considered. However, the first two states are interrelated because of the lift through the dynamic pressure and the lift coefficient. Thus, V is assumed as known and α as not known. Therefore, the unknown variables are: $\theta, \alpha, \beta, \delta_a, \delta_e, \delta_r$, and the thrust, which accounts for 7 variables. However, from the forces and moments equations, only six variables can be found. Hence, an output constraint of zero is imposed on the flight path angle, γ. Given that $\gamma = \theta - \alpha$, the number of variables to be trimmed by the procedure is adequate. This information is summarized in Table 2. [33]

Table 2 Trimming object specifications.

States	Steady State	Known
p	✓	✓
q	✓	✓
r	✓	✓
ϕ	✓	✓
θ	✓	✗
ψ	✓	✓

States	Steady State	Known
V	✓	✓
α	✓	✗
β	✓	✗
x_L	✗	✓
y_L	✓	✓
z_L	✓	✓

Inputs	Known
T	✗
δ_a	✗
δ_e	✗
δ_r	✗

Outputs	Known
γ	✓

2. Linearization

The linearization procedure involves the approximation of the nonlinear dynamics around the trim points. Thus, for each flight condition, there is a State Space (SS) representation of the form:

$$\begin{aligned} \dot{x}_\delta(t) &\approx A x_\delta(t) + B_u u_\delta(t) \\ y_\delta(t) &\approx C_y x_\delta(t) + D_{yu} u_\delta(t), \end{aligned} \tag{14}$$

where the quantities $x_\delta(t) \approx x(t) - \bar{x}$ and $u_\delta(t) \approx u(t) - \bar{u}$ approximate deviations from the operating point. The higher order terms are assumed to be zero and, by abuse of notation, the δ will be omitted when referring to the SS models. Additionally, from the complete linearized SS model, the appropriate rows and columns were selected to obtain the SP SS approximation.

III. Flight Control System Design

A. Open Loop Model

A single flight condition is used for the nominal FCS design. The operating point with a Mach number of 0.5 and an altitude of 5450 meters is chosen, which is located around the middle of the flight envelope provided. The aircraft's linearized SP dynamics, $G_{SP}(s)$, around this trim point are represented in Eq. (15). The open loop design model $G(s)$ is obtained by augmenting the G_{SP} with the first order actuator model of the elevator, $G_{\delta_e}(s)$ (see Fig. 3 and section II.B.3).

$$\begin{bmatrix} \dot{\alpha} \\ \dot{q} \end{bmatrix} = \underbrace{\begin{bmatrix} -0.601 & 0.974 \\ -1.154 & -0.748 \end{bmatrix}}_{A_{SP}} \begin{bmatrix} \alpha \\ q \end{bmatrix} + \underbrace{\begin{bmatrix} -0.141 \\ -3.198 \end{bmatrix}}_{B_{SP}} \delta_e \quad , \qquad \begin{bmatrix} n_z \\ q \end{bmatrix} = \underbrace{\begin{bmatrix} 9.655 & 0.4222 \\ 0 & 1 \end{bmatrix}}_{C_{SP}} \begin{bmatrix} \alpha \\ q \end{bmatrix} + \underbrace{\begin{bmatrix} 2.3 \\ 0 \end{bmatrix}}_{D_{SP}} \delta_e \tag{15}$$

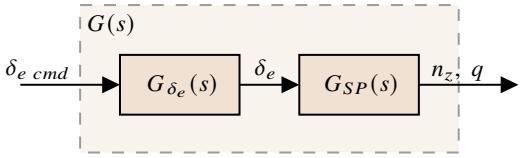

Fig. 3 Augmented open loop model, $G(s)$.

B. Design Requirements

It is fundamental to outline the goals to adequately define its design. These ensure safety and reliability of the aircraft operation by encompassing a range of critical considerations. The following specifications are considered:

(R1) Disturbance rejection at the plant input and output.
(R2) Sensor noise attenuation at the plant input and output.
(R3) Control effort reduction.
(R4) Ideal minimum classical stability gain margins (GM) and phase margins (PM) of 6 dB and 45°, respectively, for all broken loops in the plant input and outputs (soft constraint). This specification is defined as for military standards [35] which, consequently, ensures that the civil ones are also met [36].
(R5) Robustness guarantees in terms of disturbance rejection and of sensor noise and control effort attenuation in the presence of independent parametric uncertainties in the aerodynamic coefficients, varied across the range of ±30%. Stability margins shall not degrade by more than 50% of the requirements imposed in R4 in the presence of said uncertainty.
(R6) Predicted HQ within Level 1.

A fundamental control law design objective, as highlighted in requirement R6, is to achieve desirable and consistent flying qualities, even in the presence of disturbances and uncertainties. The goal is to achieve Level 1 in the Cooper-Harper Rating Scale when the controller is implemented and simulated by test pilots. For that, predicted HQ are examined. The criteria used consist of Gibson's dropback criteria (pitch rate overshoot and pitch attitude dropback) in combination with the attitude and flight path bandwidth criteria. Thus, a reference model is necessary for model following design. It is defined as a second order, as represented in Eq. (16).

$$T_{ref}(s) = \frac{C^*_{ref}(s)}{r(s)} = \frac{K_{num}(s + z_{ref})}{s^2 + 2\xi_{ref}\omega_{ref}s + \omega^2_{ref}} \tag{16}$$

Here, r corresponds to the pilot stick input signal. Taking into consideration the requirements for Class III aircraft and Category B flight phase, adequate values were selected for the SP frequency, damping, and numerator time constant [37]. Thus, to minimize control surface activity [38], the desired natural frequency was set to ω_{ref} = 1.4 rad/s, which is similar to the nominal bare airframe value (ω_{SP} = 1.25 rad/s) in the condition that will be evaluated (Ma = 0.5, h = 5450 meters). Additionally, defining the desired damping ratio as ξ = 0.75 and the numerator z_{ref} = 1.2, yields Level 1 performance in the selected HQ criteria. So that T_{ref} has unitary static gain, K_{num} = 1.6333 was selected. For this specification, a feedforward controller is used to enhance reference tracking capabilities.

C. FCS Design Configuration

1. Digital FCS

Control laws are implemented with digital FBW. There are several ways to approach digital control design. One option is to design a continuous time (CT) controller, which already takes into consideration some properties of the sampling process and computation delays in the synthesis [33]. The discrete time (DT) version of this controller yields a digital control system that performs satisfactorily under the considered sample period and digital system properties. Thus, this procedure, which is known as modified CT controller design, is used in the current research.

A general digital control scheme is represented in Fig. 4. The plant $G(s)$ is continuous and $C(z)$ is a digital controller, where s and z correspond, respectively, to the Laplace and Z-transform variables. Additionally, the Zero-Order Hold (ZOH) corresponds to a Digital-to-Analog (D/A) converter and the samplers are Analog-to-Digital (A/D) converters with a sampling time T_s. These take the samples $y_k = y(kT_s)$ and $r_k = r(kT_s)$ of the output $y(t)$ and $r(t)$, respectively, which are fed into the controller $C(z)$. Furthermore, given that in the design of the CT controller, effects of the sampling and aliasing, computational delays and hold devices are considered, these are detailed in the current section. [33]

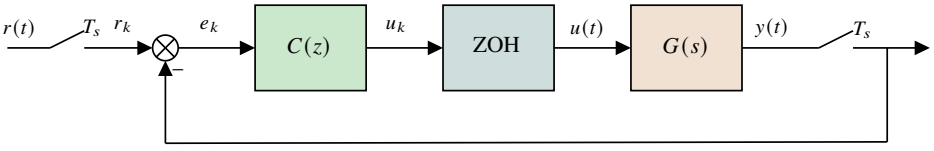

Fig. 4 General configuration of a digital controller. Based on [33].

To begin with, aliasing yields poor signal reconstruction, which might result in the misinterpretation of HF signals as LF signals [33]. To ensure aliasing does not occur, the sampling frequency ω_s should be greater than twice the highest frequency appearing in the CT signal. Nonetheless, the measurement noise also appears in the closed loop system and may not be band-limited. Thus, a low-pass anti-aliasing filter is implemented after the measuring devices and before the samplers to prevent HF measurement noise being aliased down to lower frequencies that are within the plant bandwidth.

Moreover, it is assumed that the flight control computer runs at a sampling rate, f_s, of 80 Hz, which is adopted in existing design studies [39]. Therefore, the sampling time, T_s, sampling frequency, ω_s, and Nyquist frequency, ω_N are:

$$T_s = \frac{1}{f_s} = 0.0125(s) \qquad \omega_s = 2\pi f_s = 502.65(rad/s) \qquad \omega_N = \frac{\omega_s}{2} = 251.33(rad/s) \tag{17}$$

Furthermore, the cutoff frequency of the anti-aliasing filter, ω_a, should be selected as a value lower than ω_N, in order to guarantee good attenuation beyond this frequency [33]. Thus, it was defined as in Eq. (18).

$$G_a(s) = \frac{\omega_a}{s + \omega_a}, \quad \text{where} \quad \omega_a = 150 \text{ (rad/s)} \tag{18}$$

Additionally, a computational delay of a full cycle is considered. Therefore, the variables read at t_k are used to compute the control signal applied at time t_{k+1}. The computational delay of T_s has the following transfer function:

$$G_{comp}(s) = e^{-sT_s}, \tag{19}$$

where the magnitude is unitary and the phase is $-\omega T_s$ radians. Nonetheless, given that the transfer function is not rational, Padé approximations of the exponential term are used to match the first few terms of the Taylor series expansion.

Lastly, the D/A device, implemented as a ZOH, reconstructs the plant control input $u(t)$ from the samples u_k. It has the working principle shown in Eq. (20). The expression in Eq. (21) is, therefore, the approximation with Padé terms.

$$u(t) = u(kTs) = u_k, \quad kT_s \leq t \leq (k+1)T_s \tag{20}$$

$$G_0(s) = \frac{1 - e^{-sT_s}}{sT_s} \tag{21}$$

2. C Longitudinal Control Law*

In the 1960's, the C* parameter was first introduced by Boeing [40] [41]. Although not completely successful [42], the parameter led to the creation of the C* response, which is now frequently used in commercial aviation industry as a flight control law, with variations of it being flown by different manufacturers [38]. Furthermore, although not the pure C*, several fighter aircraft, like the Lockheed Martin's F-16 and F-18 [41], have been reported to use a law of similar kind. In fact, C* controllers sometimes cover any combination of the n_z and q signals. These are usually referred to as "C*-like" approaches.

The pure C* signal is defined as a normalized sum of the pitch rate and normal acceleration at the pilot station. It is asserted that the pilots respond to a combination of these two signals, whose ratio varies according to the natural variations of the aircraft response [41]. The normal acceleration cues are intensified at higher velocities (where slight pitching produces large n_z changes), whereas the pitch rate cues are more predominant in lower velocities. Thus, a constant ratio was defined, where the relative contributions of n_z and q would automatically change based on the velocity, as a consequence of the inherent characteristics of their transfer function. Therefore, C* is described as:

$$C^* = n_z + \frac{V_{CO}}{g} q, \tag{22}$$

where g corresponds to the standard gravity and V_{CO} corresponds to the crossover velocity, where both cues would translate into equal pilot sensation. This velocity is defined to be 400 feet per second ($\approx$ 122 m/s). Therefore, the ratio is approximately equal to 12.4. This control law is followed in several publications, including [43]. Moreover, in the controller design conducted in [44], this parameter is in the feedback loop with an additional proportional gain in the pitch rate channel, which increases the damping of the SP. In [45], a proportional gain in the angle of attack signal is included in addition to the ones used in the previous formulation.

3. Signal-based $\mathcal{H}_\infty$ Synthesis - Control Layout & FCS Setup

As mentioned in section III.C.2, several configurations of the FCS are possible when using C* or C*-like approaches. This means that the integral action can be applied in the n_z signal, in q, or C*. The pure C* configuration is chosen to have a balanced disturbance rejection at LF in the signals q and n_z, while also yielding good disturbance rejection in C*.

Additionally, although many procedures compute the C* parameter with n_z measured at the PS because this signal is a reflection of how the pilot experiences the aircraft's dynamic response, this should be more closely examined. The performance signal, which is used to track a certain reference, is defined to be the C* parameter at the PS (i.e. C^*_{PS}) because it is highly related to the motions the pilots feel. However, the feedback signal, which is fundamental to providing the system robustness properties, can be a different one. It needs to be considered that:

$$n_{z_{PS}} = n_{z_{IMU}} + \frac{\dot{q}(x_{IMU\to CoG} + x_a)}{g_0}, \tag{23}$$

where $n_{z_{PS}}$ and $n_{z_{IMU}}$ are the load factors measured at the CoG and IMU, respectively. The term $x_{IMU\to CoG}$ corresponds to the distance from the IMU to the CoG location and x_a is equal to the distance between the CoG and the PS. Thus, it is decided to feedback the C* signal with the n_z measured at the IMU (i.e. C^*_{IMU}) because open loop roll-off is desired at HF to be less sensitive to structural and other sources of HF dynamics. This can be successfully achieved by not having a large derivative term in the n_z measurements which arises due to $\dot{q}$.

Figure 5 portrays the FCS configuration where, as discussed, the integral action is applied in the C^*_{IMU} signal. Additionally, the feedback controller C_{FB} provides robustness, while the feedforward controller C_{FF} improves the tracking performance. Moreover, given that the SP damping ratio for the defined flight condition is $\xi_{SP} \approx 0.54$, a SAS is implemented with a feedback gain on the pitch rate channel, C_q. The gain $K_q = 12.4$ corresponds to V_{CO}/g (see Eq. (22)). Moreover, given the digital system properties, the configuration of the system used for the design is adapted to take into account the effects of aliasing, computational delays and hold devices, as it is also observed in Fig. 5.

The inputs and outputs that are used for the control design are shown in Fig. 5 and Fig. 6. These are used to define the transfer functions that are consequently shaped via the tuning knobs of the optimization, the weighting filters. This is, therefore, a signal-based $\mathcal{H}_\infty$ design. The performance signals correspond to u, $u_{weighted}$, u_p, y_{IMU}, y_{PS}, e_{ref}, and y_{noise}. The input signals involve d_i, d_o, n, r, and r_{inner}. Additionally, the sensors introduce noise at the plant output signals n_z and q and, as observed in Fig. 6, the plant is constituted by the actuator dynamics, the SP model, and the output disturbance model $G_d(s)$, which mimics an α gust, α_g. To obtain G_d, the input matrix of the SP model $G_{SP}(s)$ (see Eq. (15)) was expanded as shown in Eq. (24), where it is assumed that α_g has the same aerodynamic effect as the

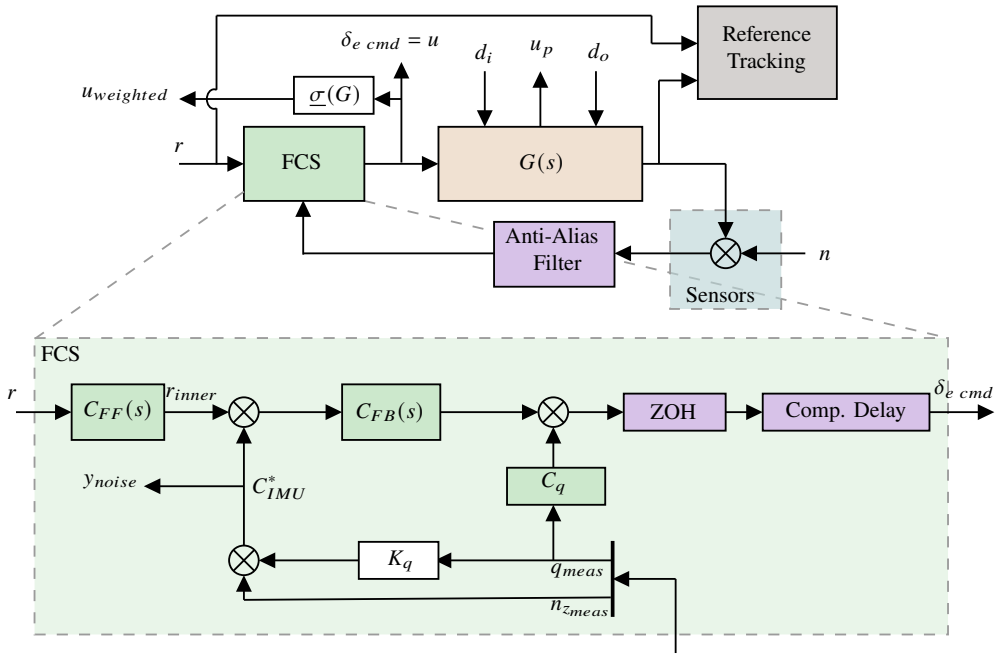

Fig. 5 FCS set up for the structured modified CT controller design.

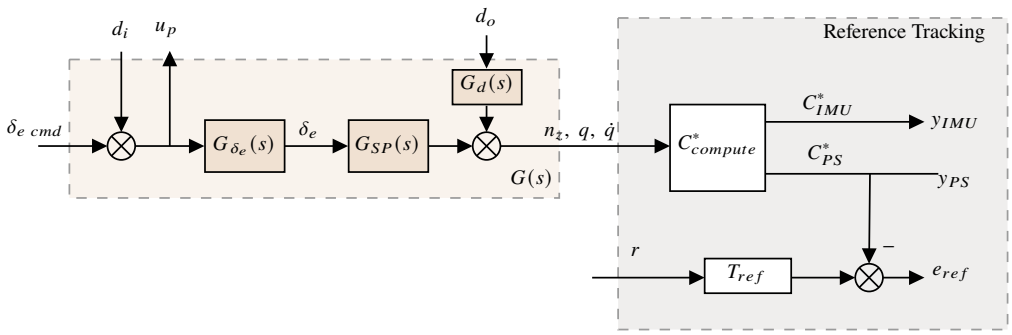

Fig. 6 Plant and reference tracking subsystems, which are expanded from Fig. 5.

variable α. Hence, G_d is obtained by considering the transfer functions from α_g to n_z and q.

$$\begin{bmatrix}\dot{\alpha}\\ \dot{q}\end{bmatrix} = \begin{bmatrix}Z_\alpha(h,Ma) & Z_q(h,Ma)\\ M_\alpha(h,Ma) & M_q(h,Ma)\end{bmatrix}\begin{bmatrix}\alpha\\ q\end{bmatrix} + \begin{bmatrix}Z_{\delta_e}(h,Ma)\\ M_{\delta_e}(h,Ma)\end{bmatrix}\delta_e - \begin{bmatrix}Z_\alpha(h,Ma)\\ M_\alpha(h,Ma)\end{bmatrix}\alpha_g \tag{24}$$

Furthermore, the reference tracking subsystem is used for the model following design, where the C* signals are retrieved with no noise. It should be noted that the plant was augmented to also output $\dot{q}$. This signal is fundamental to compute the C^*_{PS} parameter, given the transformation of n_z (refer back to Eq. (23).)

D. Constraints & Weighting Filters Selection

Moreover, shaping the Gang of Six (Go6) transfer functions ensures that the system is robust against disturbances and uncertainties. Other requirements are also achieved, namely noise attenuation, control signal reduction, and satisfactory reference tracking. Hence, for this signal-based design, the weighting filters must be specified for the optimization, as these impose the required constraints. The key aspects of their definition are discussed in this section.

1. S_o & S_i Constraints

To begin with, S_o, involves the rejection of the output disturbance d_o at the system output y_{IMU}. This constraint involves the output sensitivity $S_o = (1 + L_o)^{-1}$. The LF gain must be reduced to improve the disturbance rejection and ensure small steady state error. Using the appropriate WF W_{S_o}, the hard constraint is written as $\|W_{S_o}S_o(s)\|_\infty$. The transfer function S_o is an increasing function until it reaches its peak, which is closely linked to the degradation of the effectiveness of the attenuation and, thus, it is related to the minimum GM and PM. The peak cannot be avoided at MF [46] and it is related to the closest distance to the critical point -1 in the complex plane. Its magnitude can be translated into stability margins (SM) values as described by the disk margins (DM) expression below [47]:

$$\alpha_{max} = \frac{1}{\left\| S + \frac{\sigma - 1}{2} \right\|_\infty} \tag{25}$$

The WF inverse is selected as a high pass filter, as represented in Fig. 7. Its LF and HF gains were, respectively, selected as $\underline{k}_{S_o}$ = -50 dB and $\overline{k}_{W_{S_o}}$ = 11.6 dB. The latter value was chosen as the lowest possible to reduce the MF peak and, therefore, minimize the SM degradation. Furthermore, $\underline{\overline{k}}_{S_o}$ = 0 dB at $\underline{\overline{\omega}}_{S_o}$ = 0.2 rad/s. The higher this frequency value is, the higher the range of effectiveness of the disturbance rejection and, hence, the performance of the system when faced with output disturbances also improves.

Secondly, the input sensitivity constraint, $S_i = (1 + L_i)^{-1}$, involves the rejection of the input disturbance d_i at the plant input u_p. It should follow a similar tendency to S_o, with reduced LF gain, as portrayed in Fig. 8. Using the appropriate WF W_{S_i}, the hard constraint is written as $\|W_{S_i}S_i(s)\|_\infty$. Thus, $\underline{k}_{S_i}$ = -50 dB. Contrarily to the output disturbances, d_i is not modeled. This translates into the possibility to design a tighter filter for S_i than for S_o, resulting in $\overline{k}_{S_i}$ = 9.69 dB, $\underline{\overline{k}}_{S_i}$ = 0 dB, and $\underline{\overline{\omega}}_{S_i}$ = 5.15 rad/s.

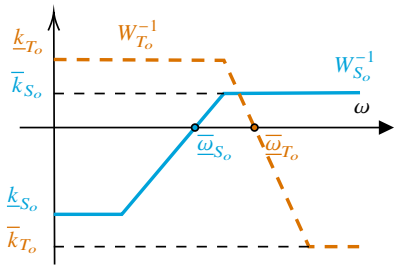

Fig. 7 Singular value shape for the desired S_o (blue) and T_o (orange) functions.

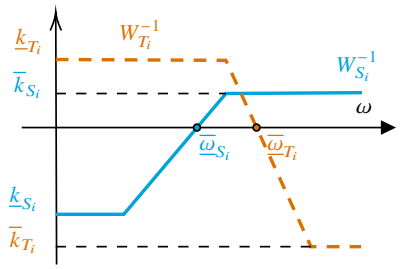

Fig. 8 Singular value shape for the desired S_i (blue) and T_i (orange) functions.

2. T_i & T_o Constraints

The constraints associated with the complementary sensitivity functions at the input and output, T_i and T_o, follow a similar tendency. These are defined as the transfer functions from d_i to the controller output u and from r_{inner} to the system output y_{IMU}, respectively. At HF, T_o contributes to noise attenuation and T_i to control signal attenuation by their low gain, which also imposes roll off in the open loops in this frequency range. Using the appropriate WF W_{T_i} and W_{T_o} as presented in Fig. 7 and Fig. 8, respectively, the hard constraints are written as $\|W_{T_i}T_i(s)\|_\infty$ and $\|W_{T_o}T_o(s)\|_\infty$. Hence, the desired low and high gain are selected equally for both transfer functions with $\underline{k}_T$ = 12.04 dB and $\overline{k}_T$ = -80 dB, respectively. Furthermore, the crossover frequencies are selected as the lowest possible which correspond to values of $\overline{\omega}_{T_i}$ = 23.4 rad/s and $\underline{\omega}_{T_o}$ = 6.4 rad/s. To improve the open loop roll off, a steeper slope is induced by increasing the order of the filter to three.

3. KS_o Constraint

The transfer function from d_o to u defines KS_o and allows to impose control signal attenuation. At LF, the transfer function is approximately equal to the inverse of the plant, and it is not dependent on the controller designer. To interpret better the attenuation level requested at MF and HF, a scaling is used for the LF by multiplying KS_o with the dcgain of the plant. Thus, the additional input to the system $u_{weighted}$ is created (see Fig. 5) to shape the transfer function KS_o. Using the appropriate WF W_{KS_o} as represented in 9, the hard constraint is written as $\|W_{KS_o}KS_o(s)\|_\infty$. Thus, $\underline{k}_{KS_o}$ = 20 dB is selected as a high value because the transfer function should not be constrained at LF. At HF, the gain must be reduced to impose noise attenuation and control signal attenuation. For that reason, $\overline{k}_{KS_o}$ = -100 dB. At $\overline{\omega}_{KS_o} \approx 10^2$ rad/s), an attenuation level of $\underline{\overline{k}}_{KS_o}$ = -30.5 dB is selected.

4. S_oG Constraint

The transfer function S_oG is selected from d_i to y_{IMU} and it is crucial to provide input disturbance rejection at the system output. It involves the plant times output sensitivity function. Once again, since disturbances are LF signals, the LF gain must be reduced. The hard constraint is written as $\|W_{S_oG}S_oG(s)\|_\infty$. From the desired singular value shape of S_oG represented in Fig. 9, $\underline{k}_{S_oG}$ = -50 dB and $\overline{k}_{S_oG}$ = 30 dB were defined. The latter value is not significant because at HF the gain of S_oG is not relevant. At $\overline{\omega}_{S_oG} = 10^{-2}$ rad/s, it is imposed $\underline{\overline{k}}_{S_oG}$ = -30.5 dB.

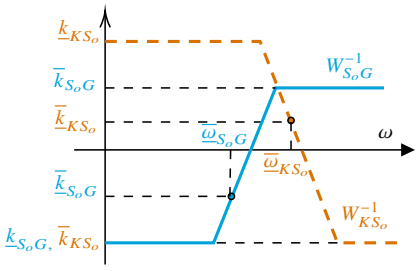

Fig. 9 Singular value shape for the desired S_oG (blue) and KS_o (orange) functions.

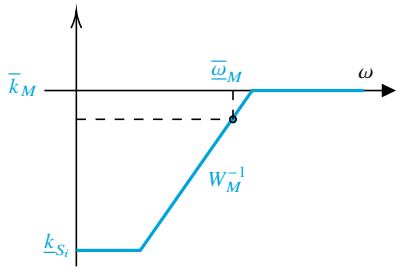

Fig. 10 Singular value shape for the desired M function.

5. M Constraint

Reference tracking is also a key requirement. To fulfill it, a model matching constraint is defined (i.e. $\|W_M M(s)\|_\infty$), which imposes low gain at LF and MF. Moreover, the lower the gain at LF, the lower is the steady state error in the response. The higher the bandwidth is, the better is the matching of the response with the ideal one imposed. However, it is a trade-off between robustness and performance. If these characteristics are improved, the parameters for the previously mentioned filters have to be worsened. A balance was achieved when considering $\underline{k}_M$ = -50 dB, $\overline{k}_M$ = -4 dB, $\underline{\overline{k}}_M$ = -23 dB, and $\overline{\omega}_M$ = 3.05 rad/s, considering the desired shape of M depicted in 10.

6. Weighting Filters Conclusions & Optimization

The filters characteristics are summarized in Table 3. The expression in Eq. (26) concludes that defining the weighting filters as the inverse of the desired shapes for each transfer function and having a γ lower or equal to unity results in the satisfaction of the gain limitations imposed.

$$\|W_{C_i}(s)C_i(s)\|_\infty < \gamma \iff \forall\omega \in \Re, |C_i(j\omega)| < \frac{\gamma}{|W_{C_i}(j\omega)|}, \tag{26}$$

where $W_C(s) = [W_{S_o}\, W_{S_i}\, W_{T_i}\, W_{T_o}\, W_{KS_o}\, W_{S_oG}\, W_M]^T$ and $C(s) = [S_o\; S_i\; T_i\; T_o\; KS_o\; S_oG\; M]^T$.

Table 3 WF characteristics for the structured modified CT controller design.

	$W_{S_o}^{-1}$	$W_{S_i}^{-1}$	$W_{T_i}^{-1}$	$W_{T_o}^{-1}$	$W_{KS_o}^{-1}$	$W_{S_oG}^{-1}$	W_M^{-1}
$\underline{k}$ (dB)	-50	-50	12.04	12.04	20	-50	-50
$\overline{\omega}$ (rad/s)	0.2	5.15	23.4	6.4	10^2	10^{-2}	3.05
$\underline{\overline{k}}$ (dB)	0	0	0	0	-13	-30.5	-23
$\overline{k}$ (dB)	11.6	9.69	-80	-80	-100	30	-4
Order	1	1	3	3	1	1	1

E. FCS Optimization Results

The optimization was conducted using the `systune` tool from the MATLAB® Control System Toolbox [48] in combination with `slTuner` that interfaces a Simulink file that mimics the system configurations represented in Fig. 5 and Fig. 6. Therefore, multi-objective/multi-model design problems are handled and structured controller synthesis is allowed. The performance levels for each of the constraints are, therefore, obtained and summarized in Table 4. Additionally, the tool optimizes individually the tuning objectives, enabling a higher design flexibility. The optimization results yield in seven performance levels, one for each transfer function constraint.

Table 4 Performance levels for each constraint for the structured modified CT controller design.

	S_o	S_i	T_i	T_o	KS_o	S_oG	M
γ	0.9981	0.9946	0.9915	0.9998	0.9900	0.9998	0.9998

The structures for the three tunable controllers were selected based on the result of a preliminary unstructured synthesis which was conducted with the $\mathcal{H}_\infty$ mixed sensitivity four block method. For that, the transfer functions S_o, S_oG, KS_o, and T_i were shaped with WF. These four goals were optimized in a combined form resulting in the optimal full-order controller. Consequently, a balanced truncation model order reduction analysis was conducted, where the fundamental dynamics for the controller were identified. Additionally, the ideal feedforward controller was computed based on T_{ref} and on the closed loop transfer function. Given the outcome of this analysis in terms of the most suitable controller structures, the structured optimization resulted in the controllers represented in Eq. (27).

$$C_{FF}(s) = \frac{1.0674(s+0.496)}{s+0.5307} \qquad C_{FB}(s) = \frac{-0.36499}{s} \qquad C_q = -3.2555 \tag{27}$$

F. Multi-Model Extension

An extension to the previous modified CT controller is conducted which consists of the multi-model design. This approach involves the development of a single controller that performs effectively across a grid of flight conditions. Moreover, the methodology for the controller design is similar to the one conducted previously, where the setup is the same as the one portrayed in Fig. 5. Nonetheless, for the current approach, a model array of state space models, which are obtained for the different flight conditions is substituted into the $G(s)$ model. Therefore, these models, whose conditions are detailed in Table 5, are used to collectively design a controller that guarantees acceptable robustness and performance over the entire set of conditions and that meets the requirements set in section III.B. The same input and output channels are used as before in order to impose the Go6 and model matching hard constraints. Thus, multi-model poses as an alternative option to gain-scheduling the entire flight envelope. Moreover, by accounting for variations in the system dynamics, this approach ensures that the controller is robust to changes in the nominal operating conditions, allowing for uncertainty in the altitude and speed of the aircraft.

Table 5 Flight conditions used for the multi-model modified CT controller design.

Model Name	Mach (-)	Altitude (m)
Ma06_h3250	0.6	3250
Ma06_h5450	0.6	5450
Ma06_h7650	0.6	7650
Ma05_h3250	0.5	3250
Ma05_h5450	0.5	5450
Ma05_h7650	0.5	7650
Ma04_h3250	0.4	3250
Ma04_h5450	0.4	5450

The weighting filters inverse follow the same tendency as before, although, in general, slightly worsened in terms of crossover frequencies and HF gain limits. Table 6 summarizes the selected values for the WF. Moreover, with the filters imposed, the performance levels obtained for each hard requirement are summarized in Table 7.

Table 6 Weighting filters characteristics for the multi-model modified CT structured controller design.

	$W_{S_o}^{-1}$	$W_{S_i}^{-1}$	$W_{T_i}^{-1}$	$W_{T_o}^{-1}$	$W_{KS_o}^{-1}$	$W_{S_oG}^{-1}$	W_M^{-1}
$\underline{k}$ (dB)	-50	-50	12.04	12.04	30	-50	-40
$\underline{\omega}$ (rad/s)	0.19	3.7	25.88	8.84	$2\cdot 10^2$	10^{-2}	14.9
$\underline{\underline{k}}$ (dB)	0	0	0	0	-28.5	-29.7	0
$\overline{k}$ (dB)	20	14.81	-80	-80	-100	30	12.04
Order	1	1	3	3	3	1	1

Table 7 Performance levels for each constraint for the multi-model modified CT structured controller design.

	S_o	S_i	T_i	T_o	KS_o	S_oG	M
γ	0.9987	0.9993	0.9992	0.9969	0.9969	0.9878	0.9992

Additionally, the controllers retrieved are represented in Eq. (28). The feedback and pitch rate controller structures are the same as the ones imposed on the modified CT controller design. However, to be able to meet the performance requirement in terms of model matching, the order of the feedforward controller was increased, becoming a second order structure.

$$C_{FF}(s) = \frac{0.69923(s^2 + 2.698s + 2.72)}{s^2 + 1.928s + 1.921} \qquad C_{FB}(s) = \frac{-0.35899}{s} \qquad C_q(s) = -2.2247 \tag{28}$$

IV. Simulation Results & Analysis

A. Uncertainty Introduction

The control system is said to be robust if it is insensitive to mismatches between the actual aircraft and the model of the system that is used to design the system. Thus, it is important to check robust stability by verifying if the system remains stable for all plants in the uncertainty set. Additionally, it is also crucial to check robust performance, which determines whether the performance specifications are met for all these plants. In this research, parametric uncertainty is considered and it is applied to the aerodynamic coefficients. Therefore, it was decided to introduce up to 30% uncertainty in the stability and control derivatives that affect the SP SS the most, which consist of C_{z_α}, C_{m_α}, C_{m_q}, and $C_{m_{\delta_e}}$. For each coefficient, 5 samples are taken and all of the combinations are tested, yielding $5^4 = 625$ combinations.

B. Model Matching & Go6 Frequency Responses

For the control system analysis, the frequency response of the model matching constraint and the time domain step response are illustrated in Fig. 11 and Fig. 12, respectively, for the nominal and the multi-model extension FCS.

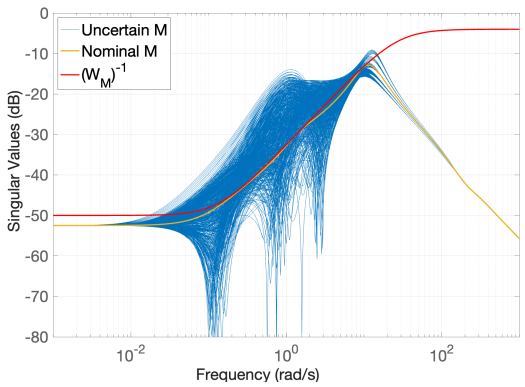

(a) Model matching M and its filter inverse.

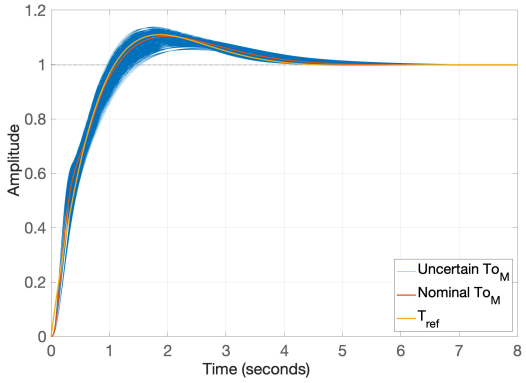

(b) Step response of the T_{ref} and To_M.

Fig. 11 Reference tracking performance, in terms of model matching frequency (Fig. 11a) and time responses (Fig. 11b) for the uncertain and nominal models, with the modified CT structured controller. To_M corresponds to the transfer function from the reference r to the signals to be tracked, C^*_{PS}.

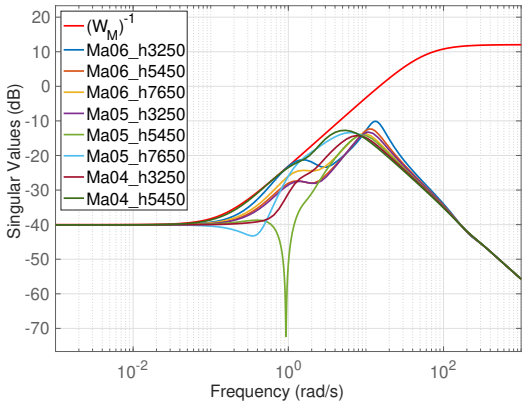

(a) Model matching M and its filter inverse.

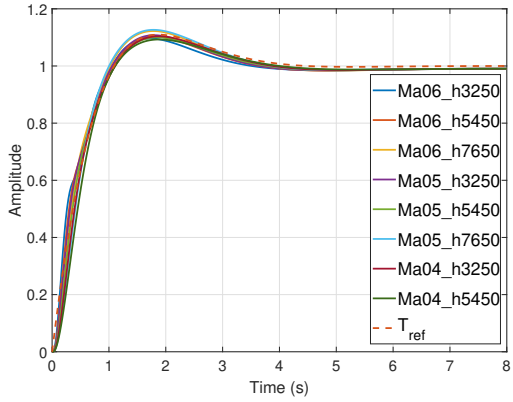

(b) Step responses of T_{ref} and To_M for each flight condition.

Fig. 12 Reference tracking performance, in terms of model matching frequency (Fig. 12a) and time responses (Fig. 12b) for each flight condition. Obtained with the multi-model digital design.

Additionally, the Go6 transfer functions are portrayed in Fig. 13. Moreover, for the analysis of the multi-model extension, the open loops broken at the plant input, $\delta_{e_{cmd}}$ and at the output C^*_{IMU} are shown in Fig. 14 for each flight condition.

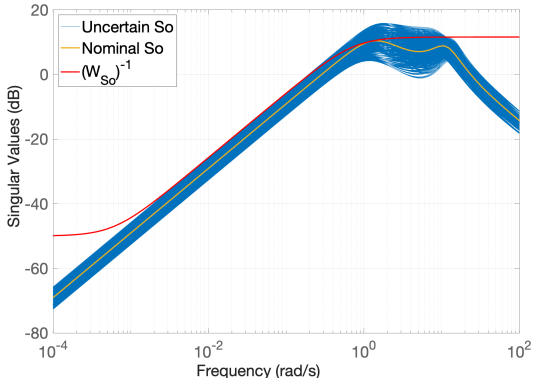

(a) Sensitivity S_o and its filter inverse, W_{So}^{-1}.

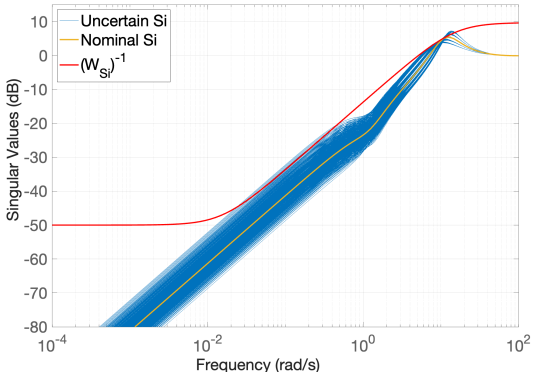

(b) Sensitivity S_i and its filter inverse, W_{Si}^{-1}.

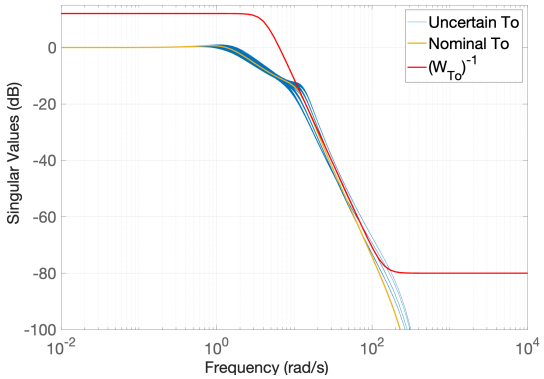

(c) Complementary sensitivity T_o and its filter inverse, W_{To}^{-1}.

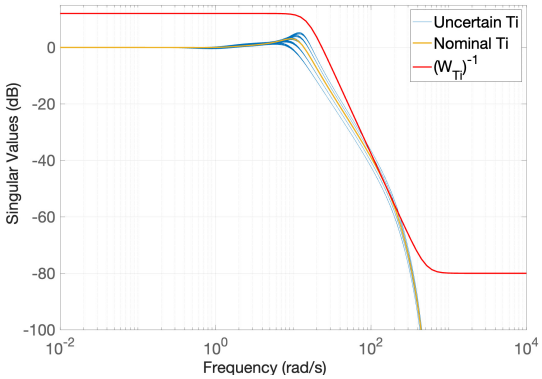

(d) Complementary sensitivity T_i and its filter inverse, W_{Ti}^{-1}.

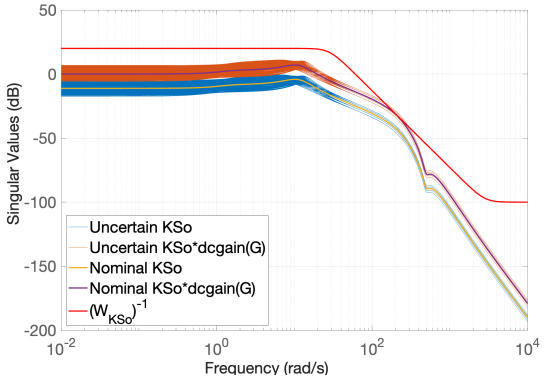

(e) Control sensitivity KS_o, KS_o scaled and its filter inverse, W_{KSo}^{-1}.

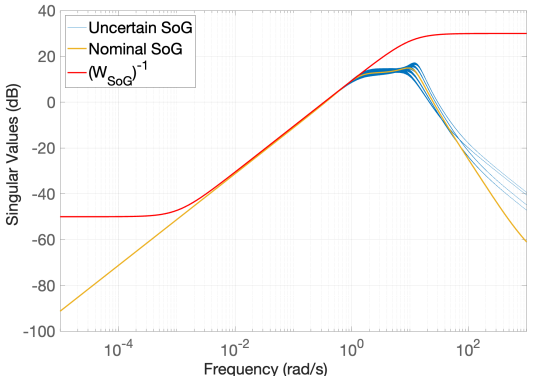

(f) S_oG and its filter inverse, W_{SoG}^{-1}.

Fig. 13 Singular Values of the Go6 closed loop trasnfer functions, namely of S_o (13a), S_i (13b), T_o (13c), T_i (13d), KS_o (13e), and S_oG (13f), with the associated weighting filters' inverse for the uncertain and nominal models. These concern the modified CT structured controller.

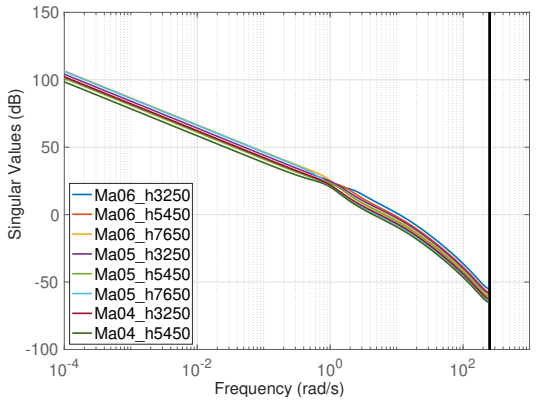

(a) Open loop at the plant input, L_i.

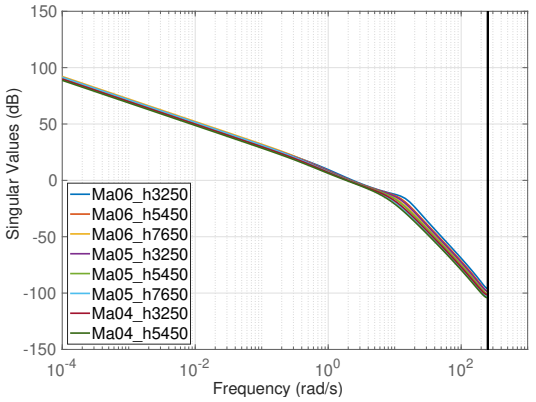

(b) Open loop at the virtual plant output C^*_{IMU}, L_{oC*}.

Fig. 14 Open loop singular values. Obtained with the multi-model digital design.

C. Stability Margins

Disk margins are a comprehensive measure of the robustness of the system since these consider concurrent perturbations in the phase and gain of the system and, thus, extend the concept of classical gain and phase margins. For five open loop locations, the DM and classical SM are computed and the results are shown for different scenarios. Firstly, in Table 8 the results are summarized for the DT controller in the nominal case, whereas, in Table 9, the worst case (WC) values are shown when uncertainty is added to the system. For the multi-model extension, the results for the flight condition with the worst values for each open loop location are shown in Table 10. Moreover, to complement the numerical evaluation the SM margins, the system's open loops are visualized on Nichols charts for the DT controller and superimposed with the WC DM region, which is shown in Fig. 15 for two open loop locations.

Table 8 Balanced disk and classical loop-at-a-time gain and phase margins for the DT controller.

Broken Loop	Disk Margins		Classical Margins	
	DGM (dB)	DPM (°)	GM (dB)	PM (°)
Plant input	± 7.43	± 43.96	17.92	48.03
Virtual plant output (C^*_{IMU})	± 12.77	± 64.10	16.93	64.20
Plant output ($n_{z_{IMU}}$)	± 16.38	± 72.74	25.87	127.76
Plant output ($n_{z_{CoG}}$)	± 13.95	± 67.32	17.04	125.07
Plant output (q)	± 6.48	± 39.23	13.62	43.42

Table 9 Worst case disk and classical loop-at-a-time gain and phase margins of the uncertain models. These concern the DT controller.

Broken Loop	WC Disk Margins		WC Classical Margins	
	DGM (dB)	DPM (°)	GM (dB)	PM (°)
Plant Input	± 6.04	± 36.96	15.11	40.26
Virtual plant output (C^*_{IMU})	± 10.05	± 55.09	14.66	56.36
Plant output ($n_{z_{IMU}}$)	± 13.19	± 65.30	17.25	122.10
Plant output ($n_{z_{CoG}}$)	± 11.45	± 60.03	13.53	118.98
Plant output (q)	± 5.13	± 32.05	11.10	35.63

Table 10 Worst case disk and classical loop-at-a-time stability margins for the multi-model controller implemented in the digital configuration.

Broke Loop	Worst Case Model Name	WC Disk Margins		WC Classical Margins	
		WC DGM (dB)	WC DPM (°)	WC GM (dB)	WC PM (°)
Plant input	Ma06_h3250	± 6.09	± 37.25	5.82	40.62
Plant output (C^*_{IMU})	Ma05_h7650	± 9.23	± 51.89	13.91	55.00
Plant output ($n_{z_{IMU}}$)	Ma06_h3250	± 14.56	± 68.81	22.29	109.72
Plant output ($n_{z_{CoG}}$)	Ma06_h3250	± 11.87	± 61.40	14.00	105.15
Plant output (q)	Ma06_h3250	± 5.03	± 31.45	10.96	34.67

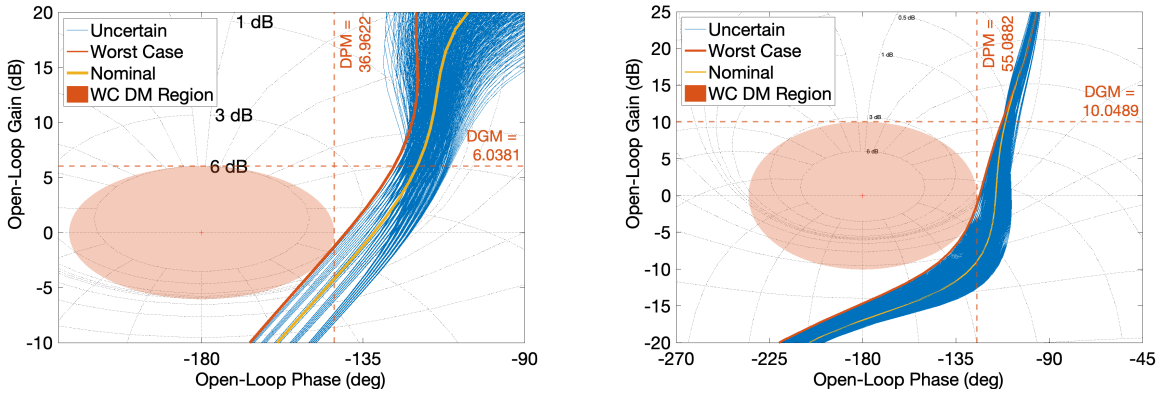

(a) Results obtained with the digital design. **(b) Results obtained with the multi-model extension.**

Fig. 15 Nichols chart and WC disk gain and phase region. Results shown for the nominal and uncertain obtained with the digital control system. Figures 15a and 15b show the input and output open loop results, respectively.

D. Handling Qualities

The dynamic characteristics of the aircraft as perceived by the pilot are evaluated with three main criteria, namely the attitude bandwidth, the pitch rate overshoot & pitch attitude dropback, and the flight path bandwidth.

1. Attitude Bandwidth

A measure of the handling qualities of an aircraft is its stability margin when operated in a CL compensatory task. Therefore, the bandwidth frequency, ω_{BW_θ} is referred to as the maximum frequency at which such CL tracking can take place without threatening stability. Thus, it is defined as the highest frequency at which the PM is at least 45° and the GM is at least 6 dB. Phase roll-off is also considered in the criteria and it is represented by a time delay, whose parameter, τ_p, can be obtained by the relation in Eq. (29) [49]. This expression is dependent on the neutral stability frequency, ω_{180}. The results for the nominal and multi-model extension are portrayed in Fig. 16.

$$\tau_p = \frac{\Delta\Phi 2\omega_{180}}{57.3(2\omega_{180})}, \tag{29}$$

2. Pitch Rate Overshoot & Pitch Attitude Dropback

Dropback is a measure of the mid-frequency response to attitude changes which, in excessive values, yield in pilot complaints of abruptness and lack of precision in pitch control [49]. While the original definition is strongly influenced by time delay [37], the definition proposed by Gibson [42] is unaffected by it. Since dropback is hypothesized as a limit in excessive mid-frequencies abruptness, it is desirable to use a parameter that is not highly influenced by time delay [49]. This parameter is already accounted for separately in the attitude bandwidth criterion. Thus, the definition proposed by Gibson [42] is used in this research. Fig. 17 shows the results for the nominal and multi-model extension.

3. Flight Path Bandwidth

The flight path response to pitch attitude change is also evaluated. The flight path bandwidth, ω_{BW_γ}, is defined as the frequency at which the response of γ lags the cockpit control input by 135°. The criteria is a function of this frequency and of the pitch attitude bandwidth, ω_{BW_θ}. Figure 18 shows the results for the nominal and multi-model extension.

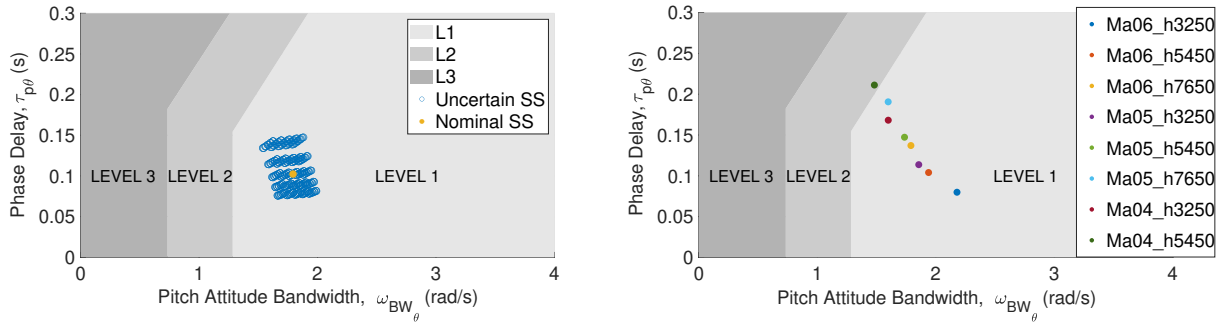

(a) Results obtained with the digital design. **(b) Results obtained with the multi-model extension.**

Fig. 16 Attitude bandwidth criteria limits, superimposed with the DT results in 16a and with the multi-model results for all flight conditions in 16b.

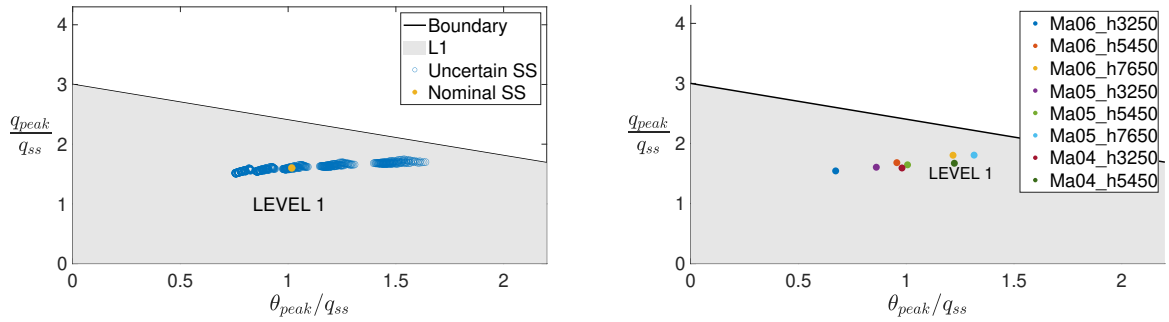

(a) Results obtained with the digital design. **(b) Results obtained with the multi-model extension.**

Fig. 17 Pitch rate overshoot and pitch attitude dropback criteria limits, superimposed with the DT results in 17a and with the multi-model results for all flight conditions in 17b.

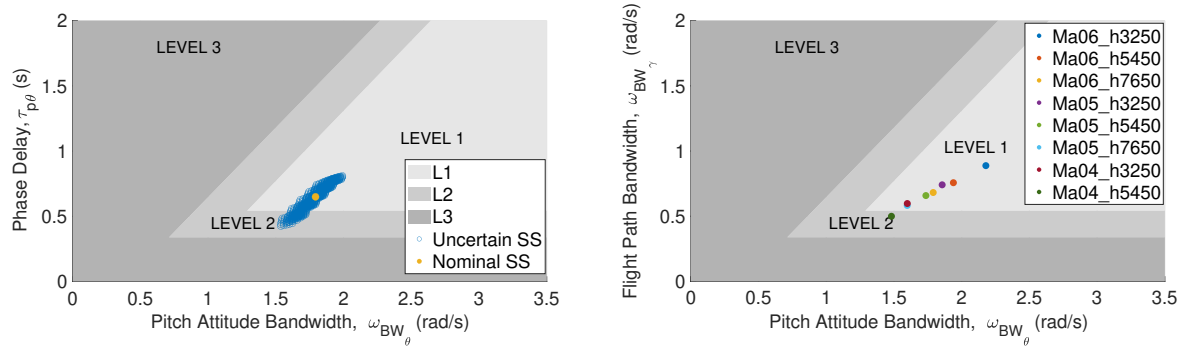

(a) Results obtained with the digital design. **(b) Results obtained with the multi-model extension.**

Fig. 18 Flight path bandwidth criteria limits, superimposed with the digital results in 18a and with the multi-model results for all flight conditions in 18b.

E. Time Domain Simulations

The FCS was implemented in the linear and nonlinear simulation model. To assess the system under realistic operating conditions, output AoA gust disturbances, step input disturbances, and measurement noise were added to the simulation. All disturbance and noise parameters used in the simulation are summarized in Table 11. The simulation results are shown in Fig. 19, when a null reference tracking is given.

Table 11 Summary of disturbances and sensor noise parameters used in simulation.

Category	Type / Signal	Description	Amplitude / Value	Time Applied	Additional Details
Output disturbance	AoA gust	Gust 1	+3 deg	t = [12,18] s	Modeled as 1-cos(α), 6 second period
		Gust 2	+7 deg	t = [30,36] s	
Input disturbance	Step input	Step 1	+2 deg	t = 6 s	Instantaneous step
		Step 2	-3 deg	t = 22 s	
Noise (white noise, high-pass filtered)	p, q, r	Variance	$\sigma^2 = 4 \cdot 10^{-7}$ rad/s	t = 40 s	Values retrieved from [50]. To verify the contribution of noise independently, this signal is only introduced at $t = 40s$.
		Bias	$3 \cdot 10^{-5}$ rad/s		
	n_x, n_y, n_z	Variance	$\sigma^2 = 1.5 \cdot 10^{-5}$ g		
		Bias	$2.5 \cdot 10^{-3}$ g		

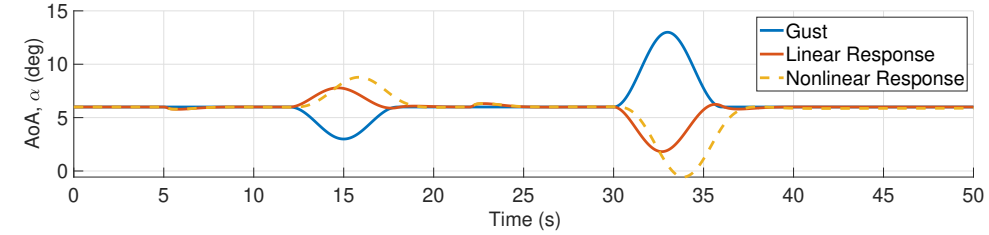

(a) System state α (angle of attack).

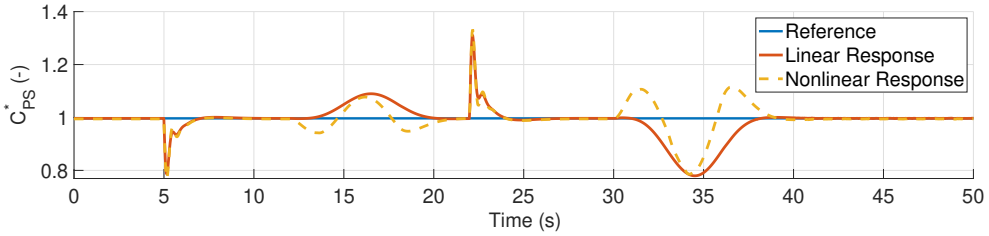

(b) Tracked output signal, C^*_{PS}.

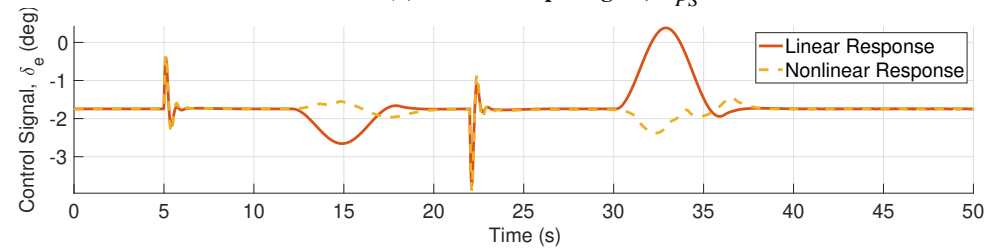

(c) Control signal, δ_e.

Fig. 19 Nonlinear simulation with the nominal digital controller. Input and output disturbances, α gusts, and noise are introduced.

Furthermore, a reference following command is given to the system and the linear and nonlinear simulation results are illustrated in Fig. 20. The nonlinear simulation results show that, toward the end of the simulation, the tracking starts deviating from the given reference. The cause for this behavior is clearly shown in Fig. 21, where the flight condition evolves to a region of the flight envelope where no valid aerodynamic data exists and which is further away from the trim point around which the control law was optimized.

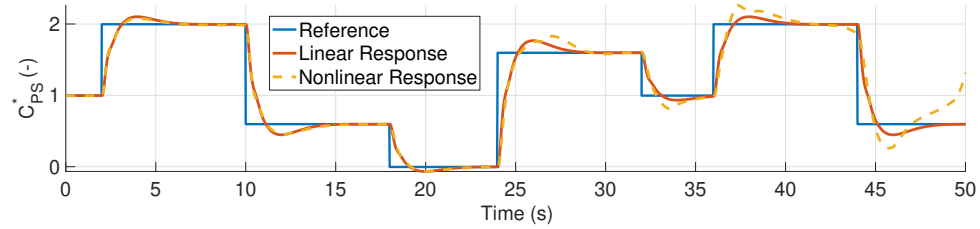

(a) Tracked output signal, C^*_{PS}.

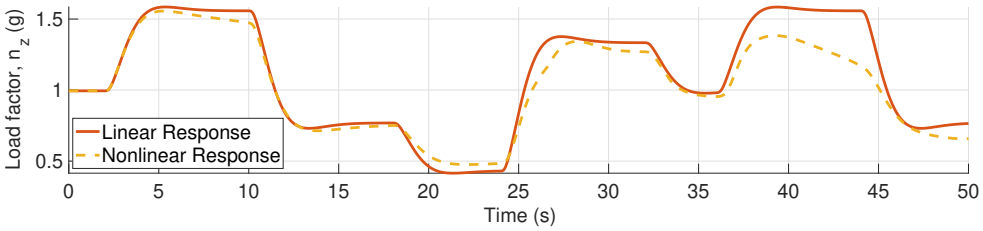

(b) System output n_z.

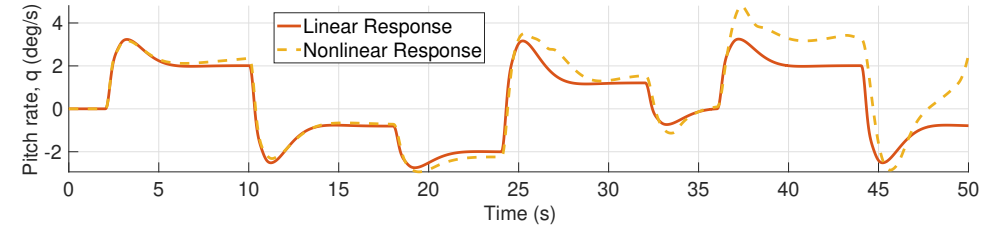

(c) System output q.

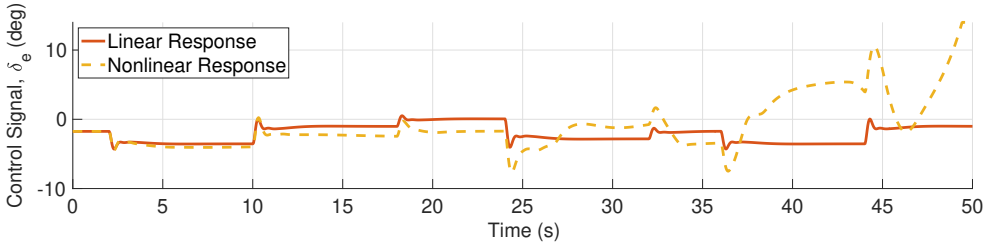

(d) Control signal, δ_e.

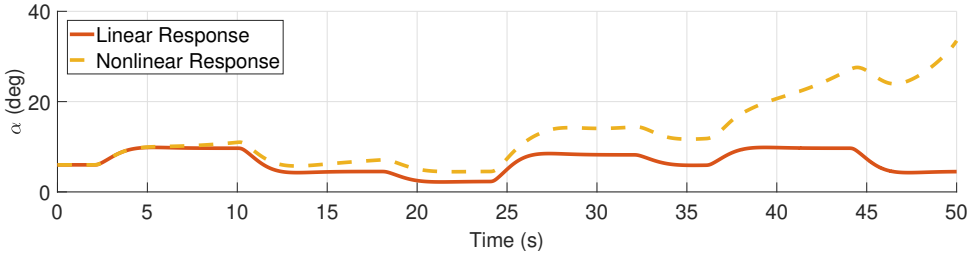

(e) System state α (angle of attack).

Fig. 20 Nonlinear simulation with the nominal digital controller.

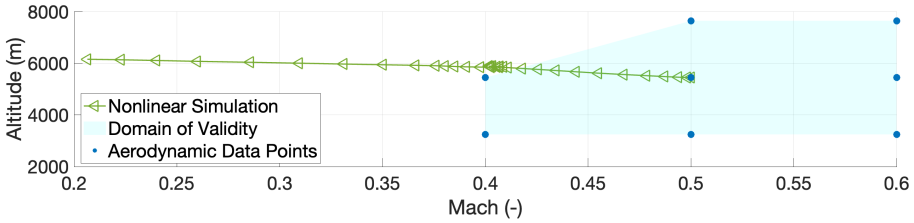

Fig. 21 Flight condition evolution for the nonlinear simulation.

To evaluate the FCS multi-model extension in the time domain, the system is tested in 82 simulations. Figure 22 shows the Mach-altitude trajectories for all runs. Each simulation is initialized at a point on the boundary of the flight envelope, indicated by red crosses. By applying a repetitive reference command, the envelope is systematically explored. The blue lines depict the evolution of the flight conditions, showing that the full region is covered. A stopping command is triggered whenever a trajectory exits the intended domain, and the blue arrows mark the end of each simulation. The objective is to verify that, when implemented on the 6-DoF nonlinear model, the controlled system performs as intended throughout the entire flight envelope. Figure 23 illustrates the time evolution of the C^*_{PS} parameter for all 82 runs under repetitive step inputs. The responses exhibit a consistent behavior across all flight conditions, which is expected and desired given that a single reference model is used in the multi-model design, despite the significant differences in the underlying dynamics at each flight point.

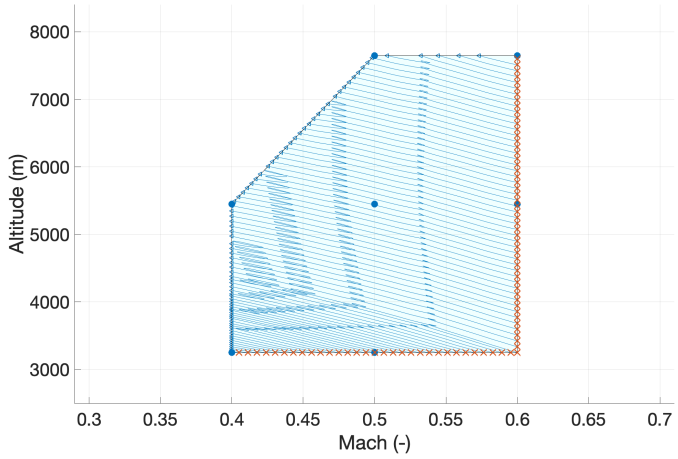

Fig. 22 Flight envelope and the Mach-altitude trajectory of 82 simulation runs on the 6 DoF model.

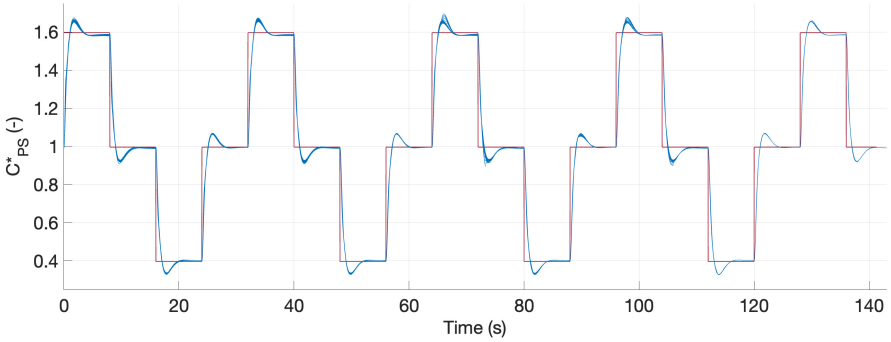

Fig. 23 C^*_{PS} parameter response for the 82 simulation runs on the 6DoF, given a repetitive reference signal.

V. Conclusion and Recommendations

This paper demonstrated the successful application of the signal-based $\mathcal{H}_\infty$ framework to the longitudinal FCS design of the Flying V concept aircraft, addressing a clear gap in prior flight control research dominated by inversion-based methods. In this work, a pure C^* control architecture was adopted, with integral action applied to the C^* signal to ensure balanced low frequency disturbance rejection in both pitch rate and normal acceleration signals. While C^* tracking was defined at the pilot station to preserve pilot-perceived dynamics, feedback was based on the IMU measured normal acceleration, yielding improved high frequency roll-off and reduced sensitivity to structural dynamics and sensor noise. The resulting digital FCS structure combines robust feedback, feedforward model following, and pitch rate stability augmentation controllers and it explicitly accounts for the digital implementation effects. Additionally, the robustness and performance design requirements were formalized into frequency-domain design constraints and enforced through appropriately shaped weighting filters, which serve as the tuning parameters of the optimization. Moreover, a multi-model extension was also designed enabling that a single controller performs effectively across a grid of flight conditions. By accounting for variations in the system dynamics, this approach ensures that the controller is robust to changes in the nominal operating conditions, allowing for uncertainty in the altitude and speed of the aircraft.

Furthermore, the nominal and multi-model FCS were evaluated in the time and frequency domains and in linear and nonlinear settings. Results demonstrated that the systems guaranteed noise attenuation, input and output disturbance rejection, stability under parametric uncertainties, satisfactory stability margins, as well as compliance with Level 1 HQ. Hence, by embedding robustness and HQ requirements directly into the synthesis process, the proposed C^* longitudinal control law provides a systematic and scalable alternative to existing approaches.

Future work should entail the addition of uncertainties on the mass, moment of inertia, and CoG location, for a more comprehensive analysis, as well as the development of a lateral-directional control law. Additionally, gain-scheduling or linear-parameter-varying approaches should be conducted to cover the flight envelope. Lastly, more extensive nonlinear assessments and piloted simulation trials should be performed.

References

[1] Martinez-Val, R., "Flying Wings. A New Paradigm for Civil Aviation?" *Acta Polytechnica*, Vol. 47, No. 1, 2007. doi:10.14311/914.

[2] Benad, J., "The Flying V - A New Aircraft Configuration for Commercial Passenger Transport," Deutscher Luft- und Raumfahrtkongress 2015, Rostock, 2015, pp. 1–8. doi:10.25967/370094.

[3] Benad, J., and Vos, R., "Design of a Flying V Subsonic Transport," *33rd Congress of the International Council of the Aeronautical Sciences, ICAS 2022, Stockholm, Sweden*, 2022. URL `https://resolver.tudelft.nl/uuid:95ea413d-d5b1-4cb2-a650-828cb106dbbd`.

[4] de Zoeten, G., Varriale, C., and Vos, R., "Flight Performance Evaluation of the Flying-V," *AIAA Aviation and Aeronautics Forum and Exposition, AIAA AVIATION Forum 2023, Article AIAA 2023-3484. American Institute of Aeronautics and Astronautics Inc. (AIAA)*, 2023. doi:10.2514/6.2023-3484.

[5] Torelli, R., Stroosma, O., Vos, R., and Mulder, M., "Piloted Simulator Evaluation of Low-Speed Handling Qualities of the Flying-V," *AIAA SciTech 2023 Forum. AIAA 2023-0907.American Institute of Aeronautics and Astronautics. National Harbor, MD Online*, 2023, p. 0907. doi:10.2514/6.2023-0907.

[6] Joosten, S., Stroosma, O., Vos, R., and Mulder, M., "Simulator Assessment of the Lateral-Directional Handling Qualities of the Flying-V," *AIAA SciTech 2023 Forum. AIAA 2023-0906. American Institute of Aeronautics and Astronautics*, 2023, p. 0906. doi:10.2514/6.2023-0906.

[7] Völker, W., Li, Y., and Van Kampen, E., "Twin-Delayed Deep Deterministic Policy Gradient for Altitude Control of a Flying-Wing Aircraft with an Uncertain Aerodynamic Model," *AIAA Scitech 2023 Forum. AIAA 2023-2678. American Institute of Aeronautics. National Harbor, MD Online*, 2023, p. 2678. doi:10.2514/6.2023-2678.

[8] van Overeem, S., Wang, X., and Van Kampen, E., "Handling Quality Improvements for the Flying-V Aircraft using Incremental Nonlinear Dynamic Inversion," *AIAA SCITECH 2023 Forum. AIAA 2023-0105. American Institute of Aeronautics and Astronautics. National Harbor, MD Online*, 2023, p. 0105. doi:10.2514/6.2023-0105.

[9] Stougie, J., Pollack, T., and Van Kampen, E., "Incremental Nonlinear Dynamic Inversion control with Flight Envelope Protection for the Flying-V," *AIAA SCITECH 2024 Forum. AIAA 2024-2565. American Institute of Aeronautics and Astronautics. Orlando, FL*, 2024, p. 2565. doi:10.2514/6.2024-2565.

[10] Traas, T., "Hybrid INDI with enhanced FEP for the Flying-V." , MSc Thesis, TU Delft, 2024. URL https://resolver.tudelft.nl/uuid:1c3fb8d1-4e7a-4bda-8ce0-537a69fe64f8.

[11] Atmaca, D., and Kampen, E. V., "Fault Tolerant Control for the Flying-V Using Adaptive Incremental Nonlinear Dynamic Inversion," *AIAA SCITECH 2025 Forum. AIAA 2025-0081. American Institute of Aeronautics and Astronautics. Orlando, FL*, 2025. doi:10.2514/6.2025-0081.

[12] Doyle, J., Glover, K., Khargonekar, P., and Francis, B., "State-Space Solutions to Standard $\mathcal{H}_2$ and $\mathcal{H}_\infty$ Control Problems," *1988 American Control Conference. Atlanta, GA, USA*, 1988, pp. 1691–1696. doi:10.23919/ACC.1988.4789992.

[13] Gahinet, P., and Apkarian, P., "A Linear Matrix Inequality Approach to $\mathcal{H}_\infty$ Control," *International Journal of Robust Nonlinear Control*, Vol. 4(4), 1994, pp. 421–448. doi:10.1002/rnc.4590040403.

[14] Apkarian, P., and Noll, D., "Nonsmooth $\mathcal{H}_\infty$ Synthesis," *IEEE Transactions on Automatic Control*, Vol. 51, No. 1, 2006, pp. 71–86. doi:10.1109/TAC.2005.860290.

[15] Gahinet, P., and Apkarian, P., "Structured $\mathcal{H}_\infty$ Synthesis in MATLAB," *IFAC Proceedings Volumes. 18th IFAC World Congress*, Vol. 44, No. 1, 2011, pp. 1435–1440. doi:10.3182/20110828-6-IT-1002.00708.

[16] Apkarian, P., and Noll, D., "The $\mathcal{H}_\infty$ Control Problem is Solved," *Aerospace Lab 13*, 2017, pp. 1–11. doi:10.12762/2017.AL13-01.

[17] Apkarian, P., Noll, D., and Rondepierre, A., "Mixed $\mathcal{H}_2/\mathcal{H}_\infty$ Control via Nonsmooth Optimization," *SIAM Journal on Control and Optimization*, Vol. 47, No. 3, 2008, pp. 1516–1546. doi:10.1137/070685026.

[18] Gahinet, P., and Apkarian, P., "Automated Tuning of Gain-scheduled Control Systems," *52nd IEEE Conference on Decision and Control. IEEE. Firenze, Italy*, IEEE, 2013, pp. 2740–2745. doi:10.1109/CDC.2013.6760297.

[19] Apkarian, P., Dao, M. N., and Noll, D., "Parametric Robust Structured Control Design," *IEEE Transactions on Automatic Control*, Vol. 60, No. 7, 2015, pp. 1857–1869. doi:10.1109/TAC.2015.2396644.

[20] Pollack, T., and van Kampen, E., "Robust Stability and Performance Analysis of Incremental Dynamic-Inversion-Based Flight Control Laws," *Journal of Guidance, Control, and Dynamics*, Vol. 46, No. 9, 2023, pp. 1785–1798. doi:10.2514/1.G006576.

[21] Sieberling, S., Chu, Q., and Mulder, J., "Robust Flight Control Using Incremental Nonlinear Dynamic Inversion and Angular Acceleration Prediction," *Journal of guidance, control, and dynamics*, Vol. 33, No. 6, 2010, pp. 1732–1742. doi:10.2514/1.49978.

[22] Papageorgiou, G., and Hyde, R. A., "Analysing the stability of NDI-based flight controllers with LPV methods," *AIAA Guidance, Navigation, and Control Conference and Exhibit. AIAA 2001-4039. American Institute of Aeronautics and Astronautics. Montreal, Canada*, 2001. doi:10.2514/6.2001-4039.

[23] Papageorgiou, G., and Polansky, M., "Tuning a Dynamic Inversion Pitch Axis Autopilot using McFarlane-Glover Loop Shaping," *Optimal Control Applications and Methods*, Vol. 30, No. 3, 2009, pp. 287–308. doi:10.1002/oca.864.

[24] Shahin, R., "Robust Flight Control for the Flying-V:Mixed μ-optimal Incremental Dynamic Inversion-based Flight Control." , MSc Thesis, TU Delft, 2024. URL https://resolver.tudelft.nl/uuid:5e0f45c7-4e3c-4648-9d72-4486af410cf4.

[25] Pedroso, B., Pollack, T., and Theodoulis, S., "Signal-Based $\mathcal{H}_\infty$ Longitudinal Controller Design for the Flying-V Aircraft," *International Federation of Automatic Control. 11th IFAC Symposium on Robust Control Design ROCOND 2025, Porto, Portugal*, Vol. 59, No. 16, 2025, pp. 80–85. doi:10.1016/j.ifacol.2025.10.083.

[26] Cappuyns, T., "Handling Qualities of a Flying V Configuration." , MSc Thesis, TU Delft, 2019. URL http://resolver.tudelft.nl/uuid:69b56494-0731-487a-8e57-cec397452002.

[27] Rubio Pascual, B., "Engine-Airframe Integration for the Flying-V." , MSc Thesis, TU Delft, 2018. URL http://resolver.tudelft.nl/uuid:75be27a7-6fd4-4112-a600-45df2999758f.

[28] van der Pluijm, R., "Cockpit Design and Integration into the Flying V." , MSc Thesis, TU Delft, 2021. URL http://resolver.tudelft.nl/uuid:da4a8d74-32fa-45f1-9f92-d01d45fdea01.

[29] van Overeem, S., Wang, X., and Van Kampen, E., "Modelling and Handling Quality Assessment of the Flying-V Aircraft," *AIAA Scitech 2022 Forum. AIAA 2022-1429. American Institute of Aeronautics and Astronautics. San Diego, CA Virtual*, 2022, p. 1429. doi:10.2514/6.2022-1429.

[30] Oosterom, W., and Vos, R., "Conceptual Design of a Flying-V Aircraft Family," *AIAA Aviation 2022 Forum. AIAA 2022-3200. American Institute of Aeronautics and Astronautics. Chicago, IL & Virtual*, 2022, p. 3200. doi:10.2514/6.2022-3200.

[31] Zipfel, P. H., *Modeling and Simulation of Aerospace Vehicle Dynamics*, 2nd ed., AIAA: American Institute of Aeronautics and Astronautics, Inc., 2007. doi:10.2514/4.862182, ISBN: 978-1-56347-875-8.

[32] Naäman, Y., "Robustness Measures in the Nonlinear Domain: Investigating Frozen-Time Robustness of Structured $\mathcal{H}_\infty$ Controllers in Nonlinear Realizations." , MSc Thesis, TU Delft, 2024. URL https://resolver.tudelft.nl/uuid:28ef6742-832a-4e39-aa6b-e9e368c498f4.

[33] Stevens, B. L., Lewis, F. L., and Johnson, E. N., *Aircraft Control and Simulation: Dynamics, Controls Design, and Autonomous Systems*, John Wiley & Sons, 2015. doi:10.1002/9781119174882, ISBN: 978-1118870976.

[34] Kim, C., Ji, C., Bang, J., Koh, G., and Choi, N., "A Survey on Structural Coupling Design and Testing of the Flexible Military Aircraft," *International Journal of Aeronautical and Space Sciences*, Vol. 25, No. 1, 2024, pp. 122–145. doi:10.1007/s42405-023-00643-y.

[35] Anonymous, "Aerospace - Flight Control Systems - General Specification for Design, Installation, and Test of Piloted Military Aircraft. SAE-AS94900." Tech. rep., SAE International, 2008.

[36] Cook, M. V., *Chapter 10 - Flying and Handling Qualities*, Butterworth-Heinemann, 2013, pp. 259–291. doi:10.1016/C2010-0-65889-5, ISBN: 978-0-08-098242-7.

[37] Anonymous, "Flying Qualities of Piloted Aircraft. MIL-HDBK-1797A," Tech. rep., U.S. Department of Defense (DoD), 1997.

[38] Favre, C., "Fly-by-Wire for Commercial Aircraft: the Airbus Experience," *International Journal of Control*, Vol. 59, No. 1, 1994, pp. 139–157. doi:10.1080/00207179408923072.

[39] Muir, E., "The HIRM Design Challenge Problem Description." *Robust Flight Control*, edited by J.-F. Magni, S. Bennani, and J. Terlouw, Berlin, Heidelberg, 1997, pp. 419–443. ISBN: 978-3-540-40941-0.

[40] Malcom, L. G., and Tobie, H. N., "New Short Period Handling Quality Criterion for Fighter Aircraft," 1965. Boeing Document No. D6-17841-T/N.

[41] Field, E., *The Application of a C* Flight Control Law to Large Civil Transport Aircraft. Technical Report No 9303*, Cranfield, England : College of Aeronautics, Cranfield Institute of Technology, 1993.

[42] Gibson, J. C., "Development of a Methodology for Excellence in Handling Qualities Design for Fly-by-Wire Aircraft," Dissertation (TU Delft), Delft University Press, 1999. URL http://resolver.tudelft.nl/uuid:6b564b35-cb74-436c-8c47-845bfbbb8b4d.

[43] Lombaerts, T., Looye, G., Ellerbroek, J., and Martin, M., "Design and Piloted Simulator Evaluation of Adaptive Safe Flight Envelope Protection Algorithm," *Journal of Guidance Control and Dynamics*, Vol. 40, 2017, pp. 1902–19024. doi:10.2514/1.G002525.

[44] Niedermeier, D., and Lambregts, A., "Fly-by-Wire Augmented Manual Control - Basic Design Considerations," *ICAS 2012-5.4.1. 28th Congress of the International Council of the Aeronautical Sciences, ICAS. Brisbane, Australia*, Vol. 4, 2012, pp. 3073–3086.

[45] Nieto-Wire, C., and Sobel, K., "Flight Control Design for a Tailless Aircraft using Eigenstructure Assignment," *International Journal of Aerospace Engineering*, Vol. 2011, No. 1, 2011, p. 549131. doi:10.1155/2011/549131.

[46] Stein, G., "Respect the Unstable," *IEEE Control Systems Magazine*, Vol. 23, No. 4, 2003, pp. 12–25. doi:10.1109/MCS.2003.1213600.

[47] Seiler, P., Packard, A., and Gahinet, P., "An Introduction To Disk Margins," *IEEE Control Systems Magazine*, Vol. 40, No. 5, 2020. doi:10.1109/MCS.2020.3005277.

[48] The MathWorks, Inc., "Control System Toolbox." , (R2025b). URL https://de.mathworks.com/help/control/, [Computer Software].

[49] Mitchell, D. G., Hoh, R. H., Aponso, B. L., and Klyde, D. H., "Proposed Incorporation of Mission-Oriented Flying Qualities into MIL-STD-1797A. WL-TR-94-3162." Tech. rep., Wright-Patterson AFB, OH, USA: Wright Laboratory, 1994.

[50] Grondman, F., Looye, G., Kuchar, R. O., Chu, Q. P., and Van Kampen, E., "Design and Flight Testing of Incremental Nonlinear Dynamic Inversion-Based Control Laws for a Passenger Aircraft," *2018 AIAA Guidance, Navigation, and Control Conference. AIAA-2018-0385. American Institute of Aeronautics and Astronautics. Kissimmee, FL, USA*, 2018, p. 0385. doi:10.2514/6.2018-0385.